European Journal of Mechanics / A Solids xxx (xxxx) xxx

Contents lists available at ScienceDirect

European Journal of Mechanics / A Solids

journal homepage: www.elsevier.com/locate/ejmsol

Lamb waves in discrete homogeneous and heterogeneous systems: Dispersion properties, asymptotics and non-symmetric wave propagation

G. Carta [a], M.J. Nieves [b,*], M. Brun [a]

[a] University of Cagliari, Department of Mechanical, Chemical and Materials Engineering, Cagliari, 09123, Italy
[b] Keele University, School of Computing and Mathematics, Keele, ST5 5BG, UK

ARTICLE INFO

On the occasion of Prof. A.B. Movchan's and Prof. N.V. Movchan's 60th birthday

Keywords:
Microstructured medium
Lamb waves
Diatomic lattice
Dispersion
Waveguide
Mode conversion

ABSTRACT

In this paper, we study Lamb waves propagating in a discrete strip, whose microstructure is represented by either a monatomic or a diatomic triangular lattice. In considering the in-plane vector problem, we derive an analytical solution for the dispersion relation of Lamb waves. Additionally, we investigate the main features of the eigenmodes of the system, which describe how the lattice strip vibrates at different frequencies. Further, we discuss how the dispersion properties depend on the number of the lattice's rows and on the chosen boundary conditions. For heterogeneous systems, we focus the attention on the internal stop-band and on the flat bands appearing in the dispersion diagram. Different asymptotic models are employed to approximate the low-frequency behaviour of the lattice strip, starting from the classical Euler–Bernoulli beam. The effective behaviour of a lattice strip with dense microstructure is also investigated, and we present a comparative numerical analysis with the analogous continuum for which the classical Lamb wave problem is posed. The theory developed is exploited here to design a structured medium capable of manipulating wavemodes, and, through conversion and selection, generating uni-directional wave phenomena. We envisage that the present work can fill a gap in the research field related to the analytical study of dispersive waves in microstructured media, whose dynamic performance is influenced by the presence of multiple external boundaries.

1. Introduction

In solid mechanics, some static and dynamic phenomena are difficult to interpret if continuous models are adopted. This is especially true in fracture problems and in the design of metamaterials, where wave phenomena at multiple scales are of primary importance. In such cases, the analysis should be based on the geometrical and constitutive properties of the microstructure rather than on the effective behaviour of the homogenised system (Kunin, 1982; Kachanov and Sevostianov, 2018; Mishuris et al., 2019).

Elastic lattices consist of periodic arrays of point masses connected by elastic ligaments. Contrarily to continuous systems, they exhibit dispersive and filtering properties even if they are homogeneous (Brillouin, 1953). A systematic analysis of two-dimensional lattice structures, providing a method to easily determine band-gaps, has been presented in Martinsson and Movchan (2003), while the effect of inclusions and defects within the microstructure on the dispersive behaviour of the system has been investigated in Movchan et al. (2006). In this context, quasi-periodic Green's functions play an important role in identifying localisation and band-gap formation in periodic structures (Movchan and Slepyan, 2007; Brun et al., 2011). Another special feature observed in discrete systems is dynamic anisotropy, leading to propagation along preferential directions even if the lattice responds isotropically in the low-frequency regime. The first demonstration of resonant star-like waveforms has been given in Ayzenberg-Stepanenko and Slepyan (2008) for scalar systems, while directionally localised waveforms for vector and flexural problems have been shown in Colquitt et al. (2012) and in McPhedran et al. (2015), respectively. Wave polarisation in vector elastic lattices, which strongly depends on the wave vector, has been characterised in Carta et al. (2019) introducing the concepts of lattice flux and lattice circulation; in this framework, in the long-wave limit, pressure and shear waves can be interpreted as circulation-free and flux-free waves, respectively.

In order to alter the dispersive and filtering characteristics of lattice structures, different types of resonators can be incorporated, as shown for instance in Tallarico et al. (2017a), Bacigalupo et al. (2019) and Vadalà et al. (2021). In particular, propagation of localised waves in a lattice with tilted resonators has been explored in Tallarico et al. (2017b). More "exotic" properties can be conferred to lattice structures by introducing active resonators. In this regard, a special role is played by gyroscopic spinners, whose effect can be exploited to tune the

* Corresponding author.
E-mail addresses: giorgio_carta@unica.it (G. Carta), m.nieves@keele.ac.uk (M.J. Nieves), michele.brun@unica.it (M. Brun).

https://doi.org/10.1016/j.euromechsol.2022.104695
Received 27 December 2021; Received in revised form 31 May 2022; Accepted 31 May 2022
Available online 18 June 2022

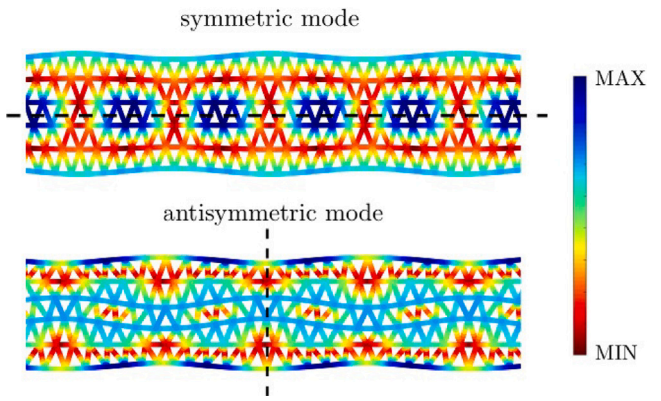

Fig. 1. Eigenmodes of a triangular lattice strip with infinite length in the horizontal direction and six rows in the vertical direction. Note that the geometry of the strip possesses no axis of symmetry in the horizontal direction. In the colour scale, blue (red) colour indicates larger (smaller) values of the total displacement field. (For interpretation of the references to colour in this figure legend, the reader is referred to the web version of this article.)

frequencies at which star-shape waveforms are generated (Brun et al., 2012; Carta et al., 2014), to create waves localised in a single line (Carta et al., 2017) and to force the uni-directional propagation of waves that are also immune to backscattering (Nash et al., 2015; Süsstrunk and Huber, 2015; Wang et al., 2015; Garau et al., 2018; Lee et al., 2018; Mitchell et al., 2018; Garau et al., 2019).

In fracture mechanics, models of elastic lattices with cracks have been developed in the literature with the aim of describing the origins of crack instability and the speed of crack propagation (Marder and Gross, 1995; Slepyan, 2002). In discrete systems, the fracture process is often manifested through the breakage of lattice bonds at a critical threshold, which introduces nonlinearity into the considered problem. Nonetheless, linear models can be employed to relate the speed of dynamic crack propagation to the dispersion curves governing waves propagating in an intact infinite lattice and semi-infinite lattice, as well as to study admissibility of the failure regimes via the solution to these linear models. Following Slepyan's work, the fracture problem is usually solved analytically by employing the Wiener–Hopf approach (Mishuris et al., 2009, 2010; Slepyan et al., 2010; Mishuris et al., 2012; Nieves et al., 2013) and asymptotic methods (Piccolroaz et al., 2009, 2010, 2012; Nieves et al., 2012), or numerically by means of finite element computations (Carta et al., 2013).

Considering the advantages that discrete structures offer with respect to their continuous counterparts, in this paper we study propagation of Lamb waves in strips of infinite length and finite width, taking full account of the internal microstructure of the strip. The latter is assumed to be made of either a monatomic or a diatomic triangular lattice. Discrete strips were previously analysed in Sharma (2017, 2018) for the scalar problem, where the lattice's particles were allowed to have a single degree of freedom in the out-of-plane direction; here, we consider the vector problem, where the displacement of each mass is a two-component vector in the lattice's plane. Illustrations of both a symmetric and an antisymmetric vibration mode of the microstructured strip considered in this paper are shown in Fig. 1. We note that while Rayleigh waves in square and triangular lattices have already been studied in the literature (in particular by Slepyan (2001a,b)), to the best of our knowledge, the analytical solution of Lamb waves propagating in microstructured strips have not been presented in previous works. In this way, we aim to fill a gap in the literature on wave propagation in discrete structures.

Furthermore, exploiting the possibility to select symmetric and antisymmetric modes of vibration, we show that the discrete strip can act as a waveguide with preferential directionality. In other words, it allows waves of a certain frequency to travel in one direction, while their propagation in the opposite direction is prevented. We note that this phenomenon was already observed in Zhu et al. (2010), where a continuous waveguide was designed. Nonetheless, the benefits of considering a discrete structure are twofold: first, a finite number of dispersion curves is exhibited by a microstructured medium; second, these dispersion curves (whose determination is essential to select the frequencies at which the effect of preferential directionality is achievable) can be obtained analytically.

The discrete strip model proposed in this work has applications in the study of the dynamic response of carbon nanotubes experiencing tension and compression due to wave propagation (Sharma, 2018) and in non-destructive evaluation methods (Diamanti et al., 2005; Su and Ye, 2021). Additionally, the theory developed here can provide a micromechanical description of dynamic phenomena propagating in elastic bodies with thin contrasting layers or substrates along the boundary (Sharma and Eremeyev, 2019; Fu et al., 2020; Kaplunov et al., 2019). Moreover, it can be useful in the dynamic study of high-contrast laminates and sandwich plates (Kaplunov et al., 2017; Aydin et al., 2018; Kaplunov et al., 2021).

The plan of the paper is as follows. In Section 2, we analyse Lamb waves in a homogeneous elastic triangular lattice, determining the dispersion relation in closed form. In the derivation we distinguish between symmetric and antisymmetric modes, and investigate the dependence of the dispersion properties of the system on the number of rows and the boundary conditions. Further, we compare the results obtained for the microstructured medium with those corresponding to the low-frequency long-wave beam approximation and to a continuum strip, where the classical Lamb problem is encountered. In Section 3, we consider a heterogeneous structure assuming that the periodic lattice has two different masses in the nodal points. This heterogeneity leads to the generation of an internal stop-band, whose dependence on the mass ratio is investigated in detail. In addition, special longitudinal and transversal eigenmodes of the diatomic discrete system are examined and discussed. In Section 4, we develop an application of the work presented in Section 3 to construct a diatomic strip capable of filtering and propagating waves of a specific type in one direction only. Finally, in Section 5, concluding remarks are provided.

2. Lamb wave propagation in an elastic homogeneous triangular lattice

We study a two-dimensional triangular array of masses M, connected by elastic springs of length L and stiffness Γ. The lattice is infinite in the x_1-direction, while it has finite size along the x_2-direction (see Fig. 2). The position of each mass is defined by the multi-index $(m,n)^{\mathrm{T}}$, where $m.n \in \mathbb{Z}$ with $0 \le n \le N$. Here, $N \in \mathbb{N}$, $N \ge 3$, with $N+1$ being the number of rows in the x_2-direction. We note that the cases $N=1$ and $N=2$ are trivial and we do not discuss them here.

The equations of motion for the lattice's particles in the x_1x_2-plane are given by

$$\begin{aligned} M\ddot{\boldsymbol{u}}^{(m,n)} = {} & \Gamma\left[\boldsymbol{a}^{(1)}\cdot\left(\boldsymbol{u}^{(m+1,n)}+\boldsymbol{u}^{(m-1,n)}-2\boldsymbol{u}^{(m,n)}\right)\boldsymbol{a}^{(1)}\right. \\ & +\boldsymbol{a}^{(2)}\cdot\left(\boldsymbol{u}^{(m+1,n-1)}+\boldsymbol{u}^{(m-1,n+1)}-2\boldsymbol{u}^{(m,n)}\right)\boldsymbol{a}^{(2)} \\ & \left.+\ \boldsymbol{a}^{(3)}\cdot\left(\boldsymbol{u}^{(m,n+1)}+\boldsymbol{u}^{(m,n-1)}-2\boldsymbol{u}^{(m,n)}\right)\boldsymbol{a}^{(3)}\right], \\ & \text{for } 0<n<N, \end{aligned} \tag{1a}$$

$$\begin{aligned} M\ddot{\boldsymbol{u}}^{(m,0)} = {} & \Gamma\left[\boldsymbol{a}^{(1)}\cdot\left(\boldsymbol{u}^{(m+1,0)}+\boldsymbol{u}^{(m-1,0)}-2\boldsymbol{u}^{(m,0)}\right)\boldsymbol{a}^{(1)}\right. \\ & +\boldsymbol{a}^{(2)}\cdot\left(\boldsymbol{u}^{(m-1,1)}-\boldsymbol{u}^{(m,0)}\right)\boldsymbol{a}^{(2)} \\ & \left.+\ \boldsymbol{a}^{(3)}\cdot\left(\boldsymbol{u}^{(m,1)}-\boldsymbol{u}^{(m,0)}\right)\boldsymbol{a}^{(3)}\right], \\ & \text{for } n=0, \end{aligned} \tag{1b}$$

$$\begin{aligned} M\ddot{\boldsymbol{u}}^{(m,N)} = {} & \Gamma\left[\boldsymbol{a}^{(1)}\cdot\left(\boldsymbol{u}^{(m+1,N)}+\boldsymbol{u}^{(m-1,N)}-2\boldsymbol{u}^{(m,N)}\right)\boldsymbol{a}^{(1)}\right. \\ & +\boldsymbol{a}^{(2)}\cdot\left(\boldsymbol{u}^{(m+1,N-1)}-\boldsymbol{u}^{(m,N)}\right)\boldsymbol{a}^{(2)} \\ & \left.+\ \boldsymbol{a}^{(3)}\cdot\left(\boldsymbol{u}^{(m,N-1)}-\boldsymbol{u}^{(m,N)}\right)\boldsymbol{a}^{(3)}\right], \\ & \text{for } n=N, \end{aligned} \tag{1c}$$

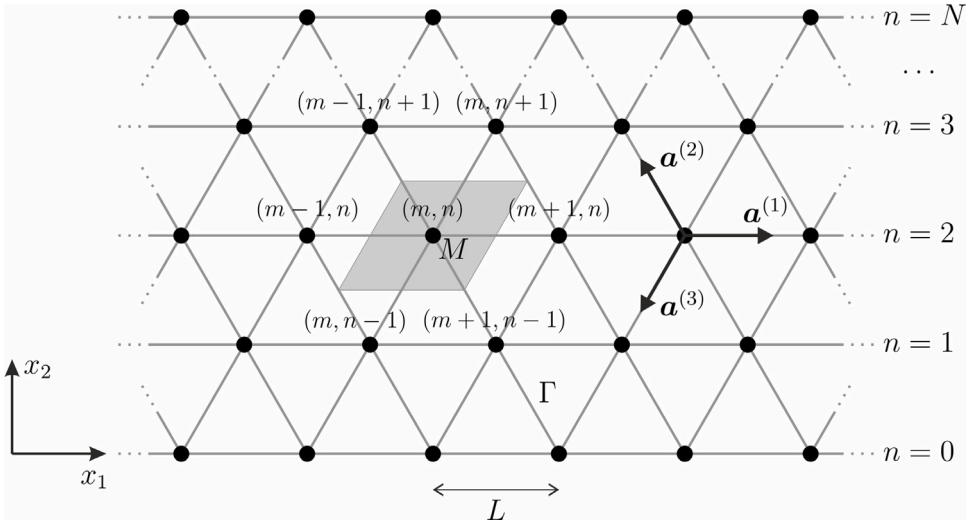

Fig. 2. Two-dimensional periodic lattice, made of identical points having mass M linked by elastic springs having stiffness Γ. The lattice is infinite in the x_1-direction and finite in the x_2-direction. In this configuration, free Neumann boundary conditions have been applied.

where $\boldsymbol{u}^{(m,n)}(t) = \left(u_1^{(m,n)}(t), u_2^{(m,n)}(t)\right)^{\mathrm{T}}$ is the displacement vector, which is a function of time t and depends on the multi-index $(m,n)^{\mathrm{T}}$. Here the dot atop of a dependent variable denotes the time derivative. Further, the vectors

$$\boldsymbol{a}^{(1)} = (1,0)^{\mathrm{T}}\,, \quad \boldsymbol{a}^{(2)} = (-1/2, \sqrt{3}/2)^{\mathrm{T}}\,, \quad \boldsymbol{a}^{(3)} = (-1/2, -\sqrt{3}/2)^{\mathrm{T}} \tag{2}$$

are used to identify the directions of the lattice's links (see Fig. 2).

Under time-harmonic conditions, the displacement vector takes the form

$$\boldsymbol{u}^{(m,n)} = \boldsymbol{U}^{(m,n)} \mathrm{e}^{\mathrm{i}\omega t}\,, \tag{3}$$

where ω is the radian frequency and $\boldsymbol{U}^{(m,n)}$ is the unknown displacement amplitude vector.

2.1. Normalisation

For the sake of simplicity, we introduce the normalised quantities

$$\boldsymbol{x} = \tilde{\boldsymbol{x}} L\,,\ \boldsymbol{u} = \tilde{\boldsymbol{u}} L\,,\ \boldsymbol{U} = \tilde{\boldsymbol{U}} L\,,\ k_1 = \tilde{k}_1 / L\,,\ t = \tilde{t}\sqrt{M/\Gamma}\,,\ \omega = \tilde{\omega}\sqrt{\Gamma/M}\,, \tag{4}$$

where the symbol tilde is used to indicate a non-dimensional quantity. In (4), $\boldsymbol{x} = (x_1, x_2)^{\mathrm{T}}$ is the position vector, while k_1 denotes the wavenumber. Additionally, $\tilde{\boldsymbol{u}}$ is assumed to be a function of the dimensionless variables $\tilde{\boldsymbol{x}}$ and $\tilde{t}$, while $\tilde{\boldsymbol{U}}$ is only $\tilde{\boldsymbol{x}}$-dependent.

For ease of notation, in the following we will omit the symbol tilde, assuming implicitly that all the variables appearing in the equations are non-dimensional.

2.2. Solution in the lattice's bulk

Employing the normalisation (4) together with (3), the governing Eqs. (1a) for the interior lattice's particles in the time-harmonic regime become

$$\begin{aligned}
&\omega^2 \boldsymbol{U}^{(m,n)} + \boldsymbol{a}^{(1)} \cdot \left(\boldsymbol{U}^{(m+1,n)} + \boldsymbol{U}^{(m-1,n)} - 2\boldsymbol{U}^{(m,n)}\right) \boldsymbol{a}^{(1)} \\
&\quad + \boldsymbol{a}^{(2)} \cdot \left(\boldsymbol{U}^{(m+1,n-1)} + \boldsymbol{U}^{(m-1,n+1)} - 2\boldsymbol{U}^{(m,n)}\right) \boldsymbol{a}^{(2)} \\
&\quad + \boldsymbol{a}^{(3)} \cdot \left(\boldsymbol{U}^{(m,n+1)} + \boldsymbol{U}^{(m,n-1)} - 2\boldsymbol{U}^{(m,n)}\right) \boldsymbol{a}^{(3)} = \boldsymbol{0} \\
&\quad \text{for } 0 < n < N\,.
\end{aligned} \tag{5}$$

The solution for the displacement amplitude vector is sought in the form

$$\boldsymbol{U}^{(m,n)} = \Lambda^n \boldsymbol{H} \mathrm{e}^{-\mathrm{i}k_1 x_1} = \Lambda^n \boldsymbol{H} \mathrm{e}^{-\mathrm{i}k_1 (m + n/2)}\,, \tag{6}$$

where $\boldsymbol{H} = \left(H_1, H_2\right)^{\mathrm{T}}$. The complex exponential represents the propagating component of the wave field in the x_1-direction, whereas Λ^n dictates the wave profile in the x_2-direction.

Substituting (2) and (6) into (5), we obtain the homogeneous system

$$\boldsymbol{A}\,\boldsymbol{H} = \boldsymbol{0}\,, \tag{7}$$

where

$$\boldsymbol{A} = \begin{pmatrix} \omega^2 - 5 + 4\cos^2\left(\frac{k_1}{2}\right) + \frac{1}{2}\left(\Lambda + \frac{1}{\Lambda}\right)\cos\left(\frac{k_1}{2}\right) & -\mathrm{i}\frac{\sqrt{3}}{2}\left(\Lambda - \frac{1}{\Lambda}\right)\sin\left(\frac{k_1}{2}\right) \\ -\mathrm{i}\frac{\sqrt{3}}{2}\left(\Lambda - \frac{1}{\Lambda}\right)\sin\left(\frac{k_1}{2}\right) & \omega^2 - 3 + \frac{3}{2}\left(\Lambda + \frac{1}{\Lambda}\right)\cos\left(\frac{k_1}{2}\right) \end{pmatrix} \tag{8}$$

(see also Slepyan (2002)). The homogeneous system (7) admits non-trivial solutions if $\det(\boldsymbol{A}) = 0$, which leads to the biquadratic equation

$$\left(\Lambda + \frac{1}{\Lambda}\right)^2 - 4p\left(\Lambda + \frac{1}{\Lambda}\right) + 4q = 0\,, \tag{9}$$

where the coefficients p and q are given by

$$\begin{aligned}
p &= \left[2\sin^2\left(\frac{k_1}{2}\right) + 1 - \frac{2\omega^2}{3}\right]\cos\left(\frac{k_1}{2}\right)\,, \\
q &= \frac{\omega^2}{3}\left\{\omega^2 - 4\left[\sin^2\left(\frac{k_1}{2}\right) + 1\right]\right\} + 3\sin^2\left(\frac{k_1}{2}\right) + 1\,.
\end{aligned} \tag{10}$$

The Eq. (9) in Λ has four solutions, denoted as $\Lambda_1, \ldots, \Lambda_4$. However, only two roots (say Λ_1 and Λ_2) are independent, since the remaining two solutions are their reciprocal quantities (namely, $\Lambda_3 = 1/\Lambda_1$ and $\Lambda_4 = 1/\Lambda_2$). The expressions for Λ_1 and Λ_2 can be written as

$$\Lambda_j = \frac{\sqrt{g_j + 1} - \sqrt{g_j - 1}}{\sqrt{g_j + 1} + \sqrt{g_j - 1}}\,, \qquad j = 1, 2\,, \tag{11}$$

where

$$g_j = p + (-1)^{j-1}\sqrt{p^2 - q}\,, \qquad j = 1, 2\,, \tag{12}$$

with $|\Lambda_j| \leq 1$, $j = 1, 2$, for $\omega \geq 0$, $k \in \mathbb{R}$.

The eigenvector $\boldsymbol{H}(\Lambda_j)$, $j = 1, 2$, is normalised such that

$$\boldsymbol{H}(\Lambda_j) = \begin{pmatrix} 1 \\ h(\Lambda_j) \end{pmatrix}\,, \tag{13}$$

$$\boldsymbol{B}_{\rm FF} = \begin{pmatrix} \boldsymbol{B}_{\rm L}(\Lambda_1)\boldsymbol{H}(\Lambda_1) & \boldsymbol{B}_{\rm L}(\Lambda_2)\boldsymbol{H}(\Lambda_2) & \boldsymbol{B}_{\rm L}(\Lambda_1^{-1})\boldsymbol{H}(\Lambda_1^{-1}) & \boldsymbol{B}_{\rm L}(\Lambda_2^{-1})\boldsymbol{H}(\Lambda_2^{-1}) \\ \Lambda_1^N \boldsymbol{B}_{\rm U}(\Lambda_1)\boldsymbol{H}(\Lambda_1) & \Lambda_2^N \boldsymbol{B}_{\rm U}(\Lambda_2)\boldsymbol{H}(\Lambda_2) & \Lambda_1^{-N} \boldsymbol{B}_{\rm U}(\Lambda_1^{-1})\boldsymbol{H}(\Lambda_1^{-1}) & \Lambda_2^{-N} \boldsymbol{B}_{\rm U}(\Lambda_2^{-1})\boldsymbol{H}(\Lambda_2^{-1}) \end{pmatrix} \tag{18}$$

Box I.

with

$$h(\Lambda_j) = \frac{\mathrm{i}\sqrt{3}\left(\Lambda_j - \frac{1}{\Lambda_j}\right)\sin\left(\frac{k_1}{2}\right)}{2\omega^2 - 6 + 3\left(\Lambda_j + \frac{1}{\Lambda_j}\right)\cos\left(\frac{k_1}{2}\right)}, \qquad j = 1, 2\,. \tag{14}$$

The displacement amplitude vector can thus be written as

$$\begin{aligned} \boldsymbol{U}^{(m,n)} = \big[&C_1 \Lambda_1^n \boldsymbol{H}\left(\Lambda_1\right) + C_2 \Lambda_2^n \boldsymbol{H}\left(\Lambda_2\right) + C_3 \Lambda_1^{-n} \boldsymbol{H}\left(\Lambda_1^{-1}\right) \\ &+ C_4 \Lambda_2^{-n} \boldsymbol{H}\left(\Lambda_2^{-1}\right)\big] \mathrm{e}^{-\mathrm{i}k_1 x_1}\,, \end{aligned} \tag{15}$$

where C_j $(j = 1, \ldots, 4)$ are unknown coefficients.

2.3. Conditions on the lattice's free boundaries

Here, we extend the validity of the relation (15) to the boundaries of the lattice strip at $n = 0$ and $n = N$. The associated procedure leads to suitable choices of the coefficients C_j, $j = 1, \ldots, 4$, to enable (1b) and (1c), in the normalised form, to be satisfied.

Note that (15) satisfies (5) for $n \in \mathbb{Z}$, i.e. without the need of any restrictions on the value of n. Therefore, using the representation (15) for $\boldsymbol{U}^{(m,0)}$ and $\boldsymbol{U}^{(m,N)}$, $m \in \mathbb{Z}$, together with (5), allows the normalised equivalents of (1b) and (1c) to be replaced by

$$\begin{aligned} &\boldsymbol{a}^{(2)} \cdot \left(\boldsymbol{U}^{(m+1,-1)} - \boldsymbol{U}^{(m,0)}\right) \boldsymbol{a}^{(2)} \\ &+\boldsymbol{a}^{(3)} \cdot \left(\boldsymbol{U}^{(m,-1)} - \boldsymbol{U}^{(m,0)}\right) \boldsymbol{a}^{(3)} = \boldsymbol{0} \qquad \text{for } n = 0\,, \end{aligned} \tag{16a}$$

$$\begin{aligned} &\boldsymbol{a}^{(2)} \cdot \left(\boldsymbol{U}^{(m-1,N+1)} - \boldsymbol{U}^{(m,N)}\right) \boldsymbol{a}^{(2)} \\ &+\boldsymbol{a}^{(3)} \cdot \left(\boldsymbol{U}^{(m,N+1)} - \boldsymbol{U}^{(m,N)}\right) \boldsymbol{a}^{(3)} = \boldsymbol{0} \qquad \text{for } n = N\,. \end{aligned} \tag{16b}$$

Physically, the conditions above represent the absence of two (out of six) elastic forces relative to the particles located at the lattice's boundaries.

Substituting (2) and (15) into (16), we derive the homogeneous system

$$\boldsymbol{B}_{\rm FF}\, \boldsymbol{C} = \boldsymbol{0}\,, \tag{17}$$

where $\boldsymbol{B}_{\rm FF}$ (Eq. (18)) is given in Box I and

$$\boldsymbol{C} = \left(C_1, C_2, C_3, C_4\right)^{\rm T}\,, \tag{19}$$

with

$$\boldsymbol{B}_{\rm L}(\Lambda_j) = \begin{pmatrix} \frac{1}{\Lambda_j}\cos\left(\frac{k_1}{2}\right) - 1 & \frac{\mathrm{i}\sqrt{3}}{\Lambda_j}\sin\left(\frac{k_1}{2}\right) \\ \frac{\mathrm{i}\sqrt{3}}{\Lambda_j}\sin\left(\frac{k_1}{2}\right) & 3\left[\frac{1}{\Lambda_j}\cos\left(\frac{k_1}{2}\right) - 1\right] \end{pmatrix}, \tag{20a}$$

$$\boldsymbol{B}_{\rm U}(\Lambda_j) = \begin{pmatrix} \Lambda_j\cos\left(\frac{k_1}{2}\right) - 1 & -\mathrm{i}\sqrt{3}\Lambda_j\sin\left(\frac{k_1}{2}\right) \\ -\mathrm{i}\sqrt{3}\Lambda_j\sin\left(\frac{k_1}{2}\right) & 3\left[\Lambda_j\cos\left(\frac{k_1}{2}\right) - 1\right] \end{pmatrix}. \tag{20b}$$

The subscript "FF" in (17) specifies that the boundary conditions are "free–free", while the subscripts "U" and "L" in (20) indicate the upper $(n = N)$ and lower $(n = 0)$ boundaries, respectively. Different boundary conditions will be considered in Section 2.7.

2.4. Dispersion curves

The dispersion relation, which shows how the radian frequency ω depends on the wavenumber k_1, is determined by imposing that $\det(\boldsymbol{B}_{\rm FF}) = 0$. The solutions of this equation are reported in Fig. 3 for a lattice with five rows $(N = 4)$. For now, we restrict subsequent computations to the case when N is even. There, the notion of symmetric and anti-symmetric modes propagating through the strip can be interpreted more naturally, owing to the structural symmetry of the medium about the row positioned at $x_2 = \sqrt{3}N/4$ $(n = N/2)$. The response of a strip with odd N is considered further in Section 2.4.2.

For each value of the wavenumber, there is a finite set of radian frequencies, equal to $2(N + 1)$. Indeed, for the specific case considered in Fig. 3, the number of dispersion curves is ten.

The dispersion diagram in Fig. 3 shows that the structure is a low-pass filter, characterised by a semi-infinite stop-band over the threshold frequency $\omega^* = 2.3932$ (the value of the 10th dispersion curve at $k_1 = \pi$), while it does not present any internal complete stop-band. In addition, there are different pairs of frequencies and wavenumbers where the group velocity is zero; hence, we expect standing waves at those points and their presence indicates regimes where waves can have positive wavenumbers and negative group velocity. Note also that the points along the dispersion curves where the group velocity is zero are connected with resonance modes for the lattice strip when subjected to an applied dynamic load at such frequencies. At these frequencies, energy is unable to propagate away from the applied load, leading to an unbounded energy density at this location in the system (Slepyan, 2002).

Along the 4th, 5th and 9th curves, there are points where the group velocity is zero in the interior of the irreducible Brillouin zone, namely for $0 < k_1 < \pi$. We note that zero group velocity points and intervals where the group velocity v_g is positive or negative along the dispersion curves, can be found from analysing the function $\mathrm{sgn}(v_g) = \mathrm{sgn}(\Omega(\omega, k))$ along the dispersion curves, where

$$\Omega(\omega, k) := -\frac{\partial[\det(\boldsymbol{B}_{\rm FF})]}{\partial k}\left(\frac{\partial[\det(\boldsymbol{B}_{\rm FF})]}{\partial \omega}\right)^{-1} \tag{21}$$

(see also Grünsteidl and Veres (2015)). Here, the expression $\Omega(\omega, k)$ is obtained by differentiating the dispersion relation $\det(\boldsymbol{B}_{\rm FF}) = 0$ along the dispersion curves. This approach provides an effective alternative for determining such information in absence of an explicit analytical expression representing the dispersion curves in terms of the frequency ω as a function of the wavenumber k_1.

2.4.1. Eigenmodes

The eigenmodes associated with the dispersion curves can be classified as either symmetric ("S") or antisymmetric ("A") (see Fig. 3). If N is even, the symmetric modes are characterised by the boundary conditions

$$U_1^{(m,0)} = U_1^{(m-N/2,N)} \quad \text{and} \quad U_2^{(m,0)} = -U_2^{(m-N/2,N)}\,, \tag{22}$$

which, using the fact that $h(\Lambda) = -h(\Lambda^{-1})$ (see Eq. (14)), lead to the following relationships among the coefficients C_j:

$$C_3 = \Lambda_1^N C_1 \qquad \text{and} \qquad C_4 = \Lambda_2^N C_2\,. \tag{23}$$

Relations (23) allow us to simplify the representation of the displacements (15) to

$$\boldsymbol{U}^{(m,n)} = \left[C_1(\Lambda_1^n \boldsymbol{I} + \Lambda_1^{N-n}\boldsymbol{X})\boldsymbol{H}\left(\Lambda_1\right) + C_2(\Lambda_2^n \boldsymbol{I} + \Lambda_2^{N-n}\boldsymbol{X})\boldsymbol{H}\left(\Lambda_2\right)\right] \mathrm{e}^{-\mathrm{i}k_1 x_1}\,, \tag{24}$$

where

$$\boldsymbol{H}(\Lambda^{-1}) = \boldsymbol{X}\,\boldsymbol{H}(\Lambda)\,, \qquad \text{with} \qquad \boldsymbol{X} = \begin{pmatrix} 1 & 0 \\ 0 & -1 \end{pmatrix}. \tag{25}$$

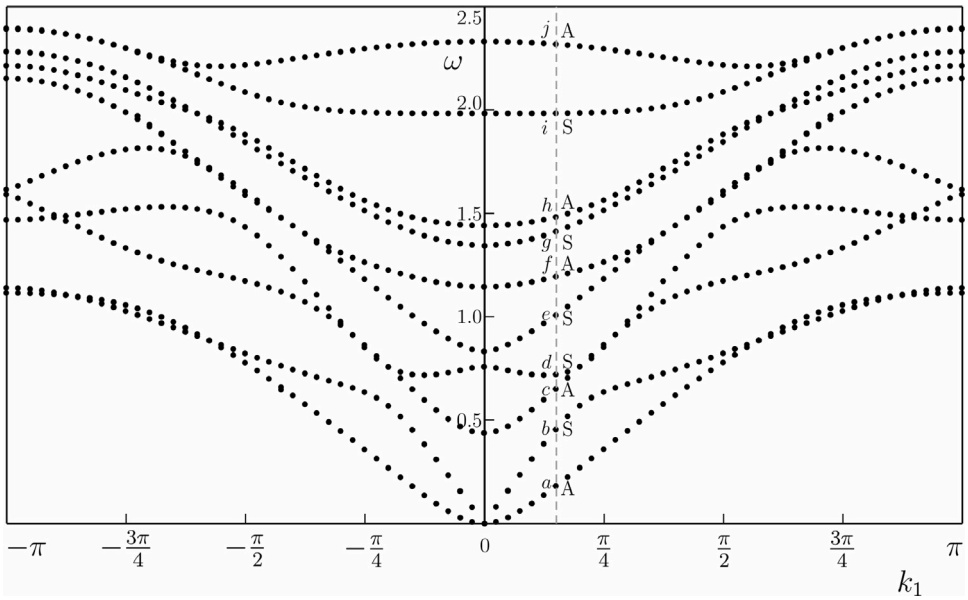

Fig. 3. Dispersion curves corresponding to Lamb waves propagating in the elastic lattice shown in Fig. 2. The lattice has five rows ($N = 4$) and free–free boundary conditions. The labels "S" and "A" indicate symmetric and antisymmetric modes, respectively, corresponding to $k_1 = 0.15\pi$ indicated by the dashed line.

Then, the homogeneous system in (17) can be reduced to a 2×2 system for only C_1 and C_2, where the Neumann boundary conditions at either $n = 0$ or $n = N$ are applied.

Conversely, a mode is antisymmetric if

$$U_1^{(m,0)} = -U_1^{(m-N/2,N)} \quad \text{and} \quad U_2^{(m,0)} = U_2^{(m-N/2,N)}. \tag{26}$$

The above conditions yield

$$C_3 = -\Lambda_1^N C_1 \qquad \text{and} \qquad C_4 = -\Lambda_1^N C_2 \tag{27}$$

and (15) takes the form

$$\boldsymbol{U}^{(m,n)} = \left[C_1(\Lambda_1^n \boldsymbol{I} - \Lambda_1^{N-n}\boldsymbol{X})\boldsymbol{H}\left(\Lambda_1\right) + C_2(\Lambda_2^n \boldsymbol{I} - \Lambda_2^{N-n}\boldsymbol{X})\boldsymbol{H}\left(\Lambda_2\right)\right] \mathrm{e}^{-\mathrm{i}k_1 x_1}. \tag{28}$$

We note similar comments hold for (28) as for (24).

Symmetric and antisymmetric modes can be visualised in Video1(a)–Video1(j), provided in the Supplementary Material accompanying this paper. In particular, the videos correspond to a fixed value of the wavenumber ($k_1 = 0.15\ \pi$) and the associated values of the radian frequency, calculated from the dispersion diagram in Fig. 3. It is clear that a harmonic external excitation with a prescribed frequency generates a response in the system that is a combination of different modes, since, in the propagating regime $0 \le \omega \lesssim \omega^*$, a horizontal line $\omega = \text{Const}$ intersects more than one dispersion curve.

2.4.2. Symmetric and antisymmetric modes for odd N

When N is odd, the full symmetry is lost, as while horizontal rows n and $N - n$, with $n = 0, \dots, (N-1)/2$, are symmetrically placed with respect to the horizontal line $x_2 = \sqrt{3}N/4$, the horizontal positions of the nodes in any two neighbouring rows are separated by $1/2$. Nevertheless, symmetric and antisymmetric modes propagate within the lattice.

In particular, symmetric modes are enforced by the conditions

$$U_1^{(m,0)} = \frac{U_1^{(m-(N+1)/2,N)} + U_1^{(m-(N-1)/2,N)}}{2} \quad \text{and}$$
$$U_2^{(m,0)} = -\frac{U_2^{(m-(N+1)/2,N)} + U_2^{(m-(N-1)/2,N)}}{2}, \tag{29}$$

for $m \in \mathbb{Z}$, which engage the arithmetic average displacements between the two adjacent nodes at $n = N$.

On the other hand, antisymmetric modes are subjected to the conditions

$$U_1^{(m,0)} = -\frac{U_1^{(m-(N+1)/2,N)} + U_1^{(m-(N-1)/2,N)}}{2} \quad \text{and}$$
$$U_2^{(m,0)} = \frac{U_2^{(m-(N+1)/2,N)} + U_2^{(m-(N-1)/2,N)}}{2}, \tag{30}$$

for $m \in \mathbb{Z}$.

Fig. 1 illustrates a symmetric and an antisymmetric wave in the lattice strip with odd $N = 5$, i.e. when the structure is not geometrically symmetric about the line $x_2 = \sqrt{3}N/4$. The symmetric mode corresponds to a frequency $\omega = 0.9499$ and wavenumber $k_1 = 0.5655$, while the antisymmetric one corresponds to $\omega = 1.055$ and the same wavenumber $k_1 = 0.5655$. By comparing the behaviour of the horizontal chains of the strip in the Figure, it is clear the medium supports symmetric and antisymmetric modes, even though the symmetric and antisymmetric conditions are not strictly satisfied by the node displacements in a way analogous to the case when N is even.

2.5. Asymptotic approximations

In this section we report different continuum approximations of the discrete structure. Within Section 2.5, we re-introduce the notation tilde to indicate normalised quantities. Such a notation will be omitted again from Section 2.6.

2.5.1. Beam approximation in the low-frequency regime

In the long-wave low-frequency limit, the discrete strip behaves like a homogeneous Euler–Bernoulli beam, whose longitudinal and flexural motions are described by the dispersion equations

$$\omega_L = \sqrt{\frac{E}{\rho}}\,|k_1| \tag{31}$$

and

$$\omega_F = \sqrt{\frac{E\,I_{\text{tot}}}{\rho\,A_{\text{tot}}}}\,k_1^2, \tag{32}$$

respectively, that involve dimensional quantities. In the formulae above, E and ρ represent the effective Young's modulus and density of the beam, while I_{tot} and A_{tot} denote the second moment of area

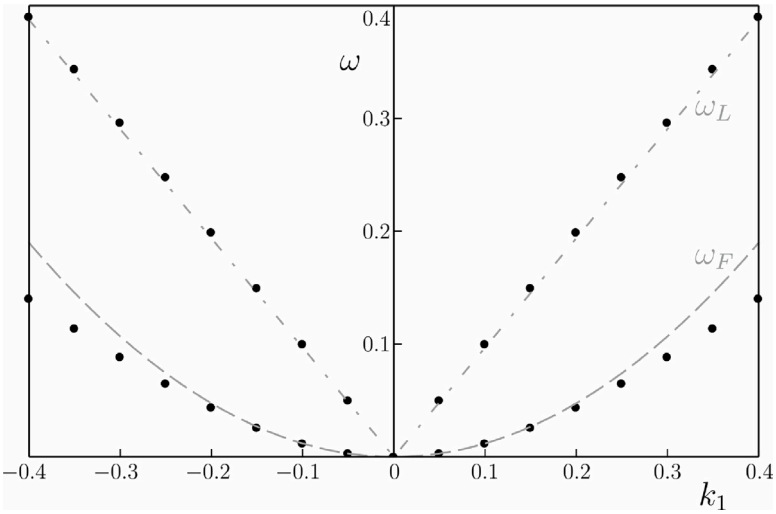

Fig. 4. Comparison between the normalised dispersion curves for the lattice strip (black dots) and for the beam approximation (grey lines), in the low-frequency, low-wavelength regime. The dashed lines refer to the flexural waves, while the dot–dashed lines are associated with the longitudinal ones.

and the area of the beam's cross-section. In order to compare the long-wave behaviours of the discrete strip and of the homogenised beam, we need to evaluate the constitutive and geometrical quantities introduced above in terms of the lattice's parameters.

The effective density is calculated by dividing the mass of each lattice's particle by the corresponding area of pertinence, represented by the grey shaded parallelogram in Fig. 2 (considering a unit thickness in the out-of-plane direction). Hence, we obtain

$$\rho = \frac{2M}{\sqrt{3}\,l^2}\,. \tag{33}$$

The Lamé parameters of an infinite triangular lattice are given by $\lambda_h = \mu_h = \sqrt{3}\,\Gamma/4$ (see Ostoja-Starzewski (2002)). Consequently, the effective Poisson's ratio is equal to

$$\nu = \frac{\lambda_h}{2(\lambda_h + \mu_h)} = \frac{1}{4}\,, \tag{34}$$

while the effective Young's modulus is given by

$$E = \frac{\mu_h(3\lambda_h + 2\mu_h)}{\lambda_h + \mu_h} = \frac{5\sqrt{3}}{8}\Gamma\,. \tag{35}$$

Looking at the geometry of the lattice's structure, the area and the second moment of area of the beam's cross-section are evaluated considering the contributions of the horizontal links, namely

$$\begin{aligned} A_{\rm tot} &= \sum_{n=0}^{N} A_n = (N+1)A\,, \quad I_{\rm tot} \simeq 2\sum_{n=0}^{N/2-1} A_i\left[\left(\frac{N}{2}-n\right)\frac{\sqrt{3}}{2}l\right]^2 \\ &= \frac{3}{2}A\,l^2\sum_{n=0}^{N/2-1}\left(\frac{N}{2}-n\right)^2\,, \end{aligned} \tag{36}$$

where $A_n = A$, the area of a single ligament, and $(N/2-n)(\sqrt{3}/2)\,l$ is the distance of the nth link from the lattice's middle row, the centre of mass of the "equivalent beam" cross-section. For the lattice shown in Fig. 2, where $N = 4$, $A_{\rm tot} = 5\,A$ and $I_{\rm tot} = 15\,A\,l^2/2$.

Substituting (33), (35) and (36) into (31) and (32), we find the dispersion relations for the beam approximating the low-frequency behaviour of the lattice strip with five rows. Using the normalisation in Section 2.1, we obtain:

$$\tilde{\omega}_L = \frac{\sqrt{15}}{4}\,|\tilde{k}_1| \quad \text{and} \quad \tilde{\omega}_F = \frac{3\sqrt{5}}{4\sqrt{2}}\tilde{k}_1^2\,. \tag{37}$$

The dispersion relations (37) are plotted in Fig. 4 with intermittent grey lines. In particular, the dashed (dot–dashed) lines correspond to the asymmetric flexural (symmetric longitudinal) waves propagating in the beam. Conversely, the black dots are the solutions of the Lamb problem in the discrete strip (see also Fig. 3). We highlight the excellent agreement between the dynamic responses of the lattice and the homogeneous beam when $\tilde{k}_1 \to 0$.

2.5.2. Homogenisation approximation for the lattice strip

If the width of the lattice strip is fixed and $N \to \infty$, the considered structured system approximates the continuum elastic strip with free boundaries. We assume that the total width of the strip is $\sqrt{3}d/2$, with $d > 0$. It follows that the associated link length in the structure is d/N. The density in terms of the lattice parameters is given by $\rho = 2MN^2/\sqrt{3}d^2$ and $\lambda_h = \mu_h = \sqrt{3}\Gamma/4$ as in Section 2.5.1. In this case, the normalised frequency and wavenumber as in (37) are related to the equivalent parameters of the continuum strip by

$$\tilde{\omega} = \sqrt{\frac{M}{\Gamma}}\,\omega_h = O(N^{-1})\,, \qquad \tilde{k}_1 = \frac{d}{N}k_h\,, \tag{38}$$

respectively. The classical dispersion curves for Lamb waves in a continuous strip, having width $D = \sqrt{3}d/2$, are identified as follows (see Graff (1975)). For symmetric modes, they are found as solutions of

$$\frac{\tanh(\gamma_s D/2)}{\tanh(\gamma_p D/2)} - \frac{4\gamma_s\gamma_p k_h^2}{(k_h^2+\gamma_s^2)^2} = 0\,, \tag{39}$$

where

$$\gamma_p^2 = k_h^2 - \frac{\omega_h^2}{c_p^2}\,, \qquad \gamma_s^2 = k_h^2 - \frac{\omega_h^2}{c_s^2}\,, \tag{40}$$

with

$$c_s = \sqrt{\frac{\mu_h}{\rho}} \qquad \text{and} \qquad c_s = \sqrt{\frac{\lambda_h + 2\mu_h}{\rho}}\,. \tag{41}$$

The associated solutions are shown as black curves in Fig. 5 and labelled with "S". Here, the computations have been performed for a continuum strip with width $d = 1$ m, density $\rho = 1$ kg m^{-3} and Lamé parameters $\lambda_h = \mu_h = \sqrt{3}/4$ Pa. Conversely, antisymmetric modes for the continuum strip are determined from

$$\frac{\tanh(\gamma_s D/2)}{\tanh(\gamma_p D/2)} - \frac{(k_h^2+\gamma_s^2)^2}{4\gamma_s\gamma_p k_h^2} = 0 \tag{42}$$

and they are shown as grey lines in Fig. 5 and labelled with "A".

In particular, using the asymptotic model discussed in Section 2.5.1, the lowest two curves found from (39) and (42) can be approximated by (31) and (32) when taking $N \to \infty$. In this limit, we obtain the

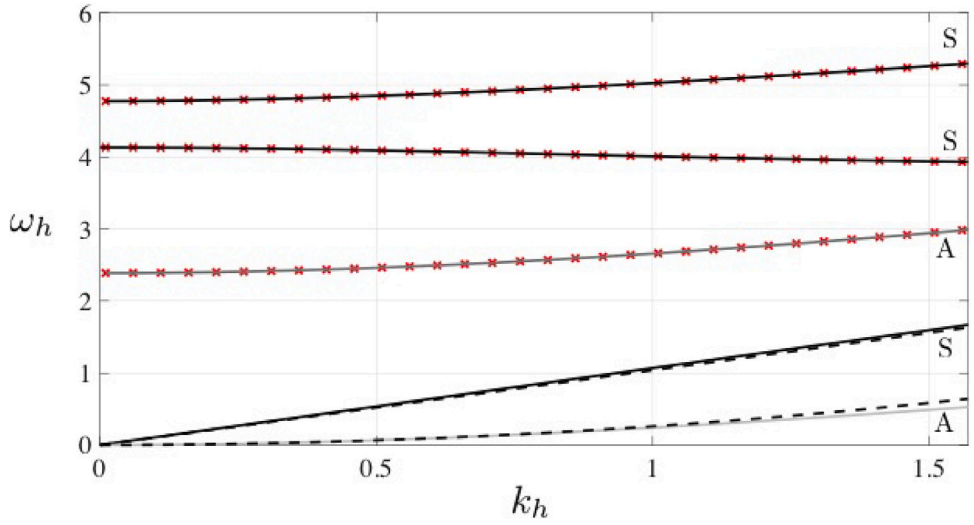

Fig. 5. Dispersion diagram for a homogeneous continuum strip, with frequency and wavenumber parameters ω_h and k_h, respectively, based on (39) (black curves) and (42) (grey curves). The two lowest curves are approximated by the functions in (43) (dashed lines) and higher curves (red crosses) by the asymptotics of the dispersion relation obtained from (17) as in (44). The continuum strip is assumed to have width $d = 1$ m, density $\rho = 1$ kg m^{-3} and the Lamé parameters $\lambda_h = \mu_h = \sqrt{3}/4$ Pa. See Section 2.5.2 for more details.

dispersion curves:

$$\omega_h^L = \sqrt{\frac{E}{\rho}}\,|k_h| \qquad \text{and} \qquad \omega_h^F = \frac{d}{4}\sqrt{\frac{E}{\rho}}\,k_h^2\,, \tag{43}$$

as $I_{\rm tot} = A_{\rm tot}\,d^2/16$, while the Young's modulus is given by (35).

High-frequency dispersion curves are then easily traceable from the asymptotics of the dimensionless dispersion relation of (17) when $N \to \infty$. For $\tilde{k}_1 \to 0$, the dispersion relation admits the asymptotic representation

$$\det(\boldsymbol{B}_{\rm FF}) \sim \sum_{j=0}^{3} T_j(\tilde{\omega})\tilde{k}_1^{2(j-1)}\,, \tag{44}$$

where $\boldsymbol{B}_{\rm FF}$ is defined in (18) and the coefficients T_j in this expansion are not reported here for brevity. We then insert (38) into the leading term in the above right-hand side and allow $N \to \infty$. The resulting leading order term is then taken and equated to zero to find the approximations to high-frequency dispersion curves in terms of dimensional variables.

The associated results appear as red crosses in Fig. 5. We note the excellent agreement between the behaviour of the curves based on (39), (42) and (43) and the asymptotics of the dispersion relation based on (17). The computations of Fig. 5 show the strip can be approximated by an Euler–Bernoulli beam at low-frequencies, whereas at higher frequencies the overall behaviour of the dense lattice strip is engaged in determining the motion of the system.

2.6. Dependence of the dispersion diagram on the number of rows

The number of dispersion curves, equal to $2(N+1)$, increases linearly with the number of lattice's rows.

In order to demonstrate the statement above with numerical examples, in Fig. 6(a) and (b) we have reported the dispersion diagrams for a lattice with seven rows ($N = 6$) and nine rows ($N = 8$), respectively. Comparing Figs. 3 and 6, we observe that the threshold frequency ω^* of the semi-infinite stop-band increases with N slightly: $\omega^* = 2.3932$ for $N = 4$, $\omega^* = 2.4196$ for $N = 6$ and $\omega^* = 2.4312$ for $N = 8$. Hence, the additional curves appearing with increasing N cluster inside the almost unaltered pass-band of the system.

In the limit when $N \to \infty$, if the distance between the rows is kept fixed, Lamb waves degenerate into Rayleigh waves, localised near the boundaries. From a physical point of view, this is obvious since the strip becomes a semi-infinite lattice structure occupying the domain $x_2 \geq 0$. From a mathematical point of view, when N becomes large, the rank of the system $\boldsymbol{B}_{\rm FF}$ reduces to 2, providing the conditions for the coefficients C_3 and C_4 to be set to zero to eliminate the exponential growth in the constructed solution (15) as $N \to \infty$ (as $|\Lambda_j| < 1$, $j = 1, 2$, in the problem for Rayleigh waves). To see this, first we recall the following relationships

$$h(\Lambda^{-1}) = -h(\Lambda) \qquad \text{and} \qquad \boldsymbol{B}_{\rm U}(\Lambda^{-1})\boldsymbol{H}(\Lambda^{-1}) = \boldsymbol{X}\boldsymbol{B}_{\rm L}(\Lambda)\boldsymbol{H}(\Lambda) \tag{45}$$

and insert them into (18). From there, the coefficients C_j, $j = 1, \dots, 4$, can be obtained by analysing the degeneracies of the matrix

$$\boldsymbol{B}_{\rm FF} = \begin{pmatrix} \boldsymbol{Q}(\Lambda_1, \Lambda_2) & \boldsymbol{Q}(\Lambda_1^{-1}, \Lambda_2^{-1}) \\ \boldsymbol{O} & \boldsymbol{Q}(\Lambda_1, \Lambda_2)\boldsymbol{\Lambda}^{-N} - \boldsymbol{Q}(\Lambda_1^{-1}, \Lambda_2^{-1})\boldsymbol{\Lambda}^{N}[\boldsymbol{Q}(\Lambda_1, \Lambda_2)]^{-1}\boldsymbol{Q}(\Lambda_1^{-1}, \Lambda_2^{-1}) \end{pmatrix}, \tag{46}$$

where $\boldsymbol{O}$ is the zero 2×2-submatrix,

$$\boldsymbol{Q}(\Lambda_1, \Lambda_2) = [\boldsymbol{B}_{\rm L}(\Lambda_1)\boldsymbol{H}(\Lambda_1), \boldsymbol{B}_{\rm L}(\Lambda_2)\boldsymbol{H}(\Lambda_2)] \qquad \text{and} \qquad \boldsymbol{\Lambda} = \text{diag}(\Lambda_1, \Lambda_2)\,. \tag{47}$$

When $N \to \infty$, $\boldsymbol{\Lambda}^N \to \boldsymbol{O}$, the system (17) can be reduced to the equivalent form

$$\begin{pmatrix} \boldsymbol{Q}(\Lambda_1, \Lambda_2) & \boldsymbol{Q}(\Lambda_1^{-1}, \Lambda_2^{-1}) \\ \boldsymbol{O} & \boldsymbol{Q}(\Lambda_1, \Lambda_2)\boldsymbol{\Lambda}^{-N} \end{pmatrix}\boldsymbol{C} = \boldsymbol{0}\,. \tag{48}$$

Considering that $\det(\boldsymbol{\Lambda}) \neq 0$, the degenerate frequencies and wavenumbers of this system are then found from

$$\det\left[\boldsymbol{Q}(\Lambda_1, \Lambda_2)\right] = 0\,. \tag{49}$$

Here, $\boldsymbol{Q}(\Lambda_1, \Lambda_2)$ provides the eigensolutions associated with the Rayleigh waves propagating in the neighbourhood of the lower boundary ($n = 0$) in the lattice half-plane. This matrix function is also given in Slepyan (2002). The coefficients C_j, $j = 1, \dots, 4$, are not uniquely determined, but they can be derived setting $C_3 = C_4 = 0$, based on physical considerations.

2.7. Different boundary conditions

The approach presented above can be applied to analyse wave propagation in lattice strips with different constraints on the boundary. In the following, we briefly describe the case of Dirichlet and mixed-type boundary conditions.

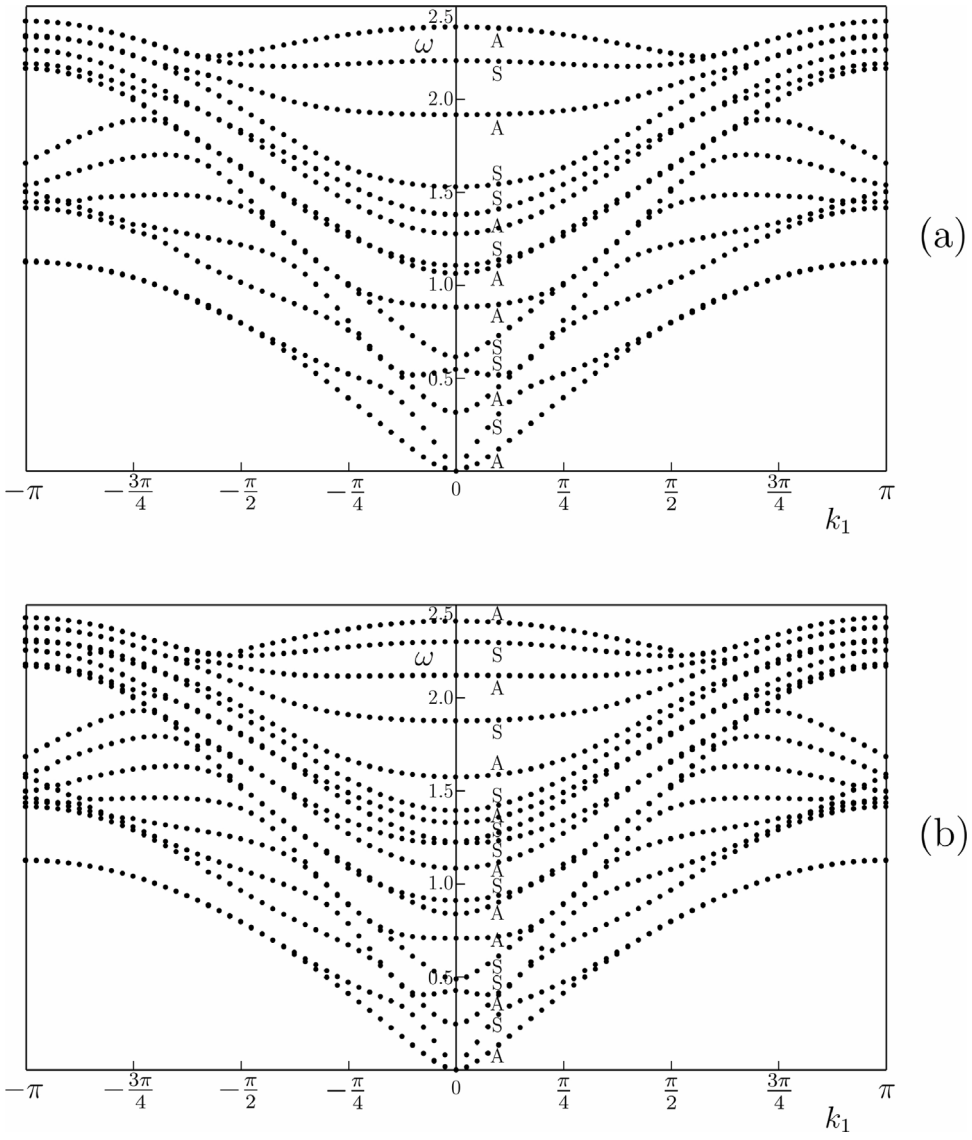

Fig. 6. Dispersion curves associated with Lamb waves for homogeneous triangular lattices with free–free boundary conditions, having (a) $N = 6$ and (b) $N = 8$. The labels "S" and "A" indicate symmetric and antisymmetric modes, respectively.

2.7.1. Clamped–clamped boundary conditions

Now we assume that null Dirichlet conditions are applied at the boundaries of the lattice. Therefore, we impose:

$$\boldsymbol{U}^{(m,0)} = \boldsymbol{0} \qquad \text{for } n = 0\,, \tag{50a}$$

$$\boldsymbol{U}^{(m,N)} = \boldsymbol{0} \qquad \text{for } n = N\,. \tag{50b}$$

After substituting (2) and (15) into (50), we obtain the following homogeneous system:

$$\boldsymbol{B}_{\mathrm{CC}}\,\boldsymbol{C} = \boldsymbol{0}\,, \tag{51}$$

where

$$\boldsymbol{B}_{\mathrm{CC}} = \begin{pmatrix} 1 & 1 & 1 & 1 \\ h\left(\Lambda_1\right) & h\left(\Lambda_2\right) & h\left(\Lambda_1^{-1}\right) & h\left(\Lambda_2^{-1}\right) \\ \Lambda_1^{N} & \Lambda_2^{N} & \Lambda_1^{-N} & \Lambda_2^{-N} \\ \Lambda_1^{N} h\left(\Lambda_1\right) & \Lambda_2^{N} h\left(\Lambda_2\right) & \Lambda_1^{-N} h\left(\Lambda_1^{-1}\right) & \Lambda_2^{-N} h\left(\Lambda_2^{-1}\right) \end{pmatrix}, \tag{52}$$

while $\boldsymbol{C}$ is the vector of unknown coefficients given by (19). The subscript "CC" in (52) indicates that the boundary conditions are of the "clamped–clamped" type in this scenario.

Non-trivial solutions are determined from the condition that $\det\left(\boldsymbol{B}_{\mathrm{CC}}\right) = 0$. This leads to the dispersion curves plotted in Fig. 7(a), where a lattice with five rows has been considered. Since the nodes along the lowest and upper rows are constrained, the total number of dispersion curves is $2(N-1)$ (six in the case examined in Fig. 7(a)). Further, we note that the constraints at the boundaries cause the appearance of a low-frequency stop-band, namely waves cannot propagate through the discrete strip in the frequency range below the lowest dispersion curves.

2.7.2. Clamped–free boundary conditions

Finally, we consider mixed boundary conditions, namely zero displacements in the nodes located along the lowest row ($n = 0$) and free conditions in the upper row ($n = N$) of the lattice:

$$\begin{aligned} &\boldsymbol{U}^{(m,0)} = \boldsymbol{0} && \text{for } n = 0\,, \\ &\boldsymbol{a}^{(2)} \cdot \left(\boldsymbol{U}^{(m-1,N+1)} - \boldsymbol{U}^{(m,N)}\right) \boldsymbol{a}^{(2)} \\ &\quad + \boldsymbol{a}^{(3)} \cdot \left(\boldsymbol{U}^{(m,N+1)} - \boldsymbol{U}^{(m,N)}\right) \boldsymbol{a}^{(3)} = \boldsymbol{0} && \text{for } n = N\,. \end{aligned} \tag{53}$$

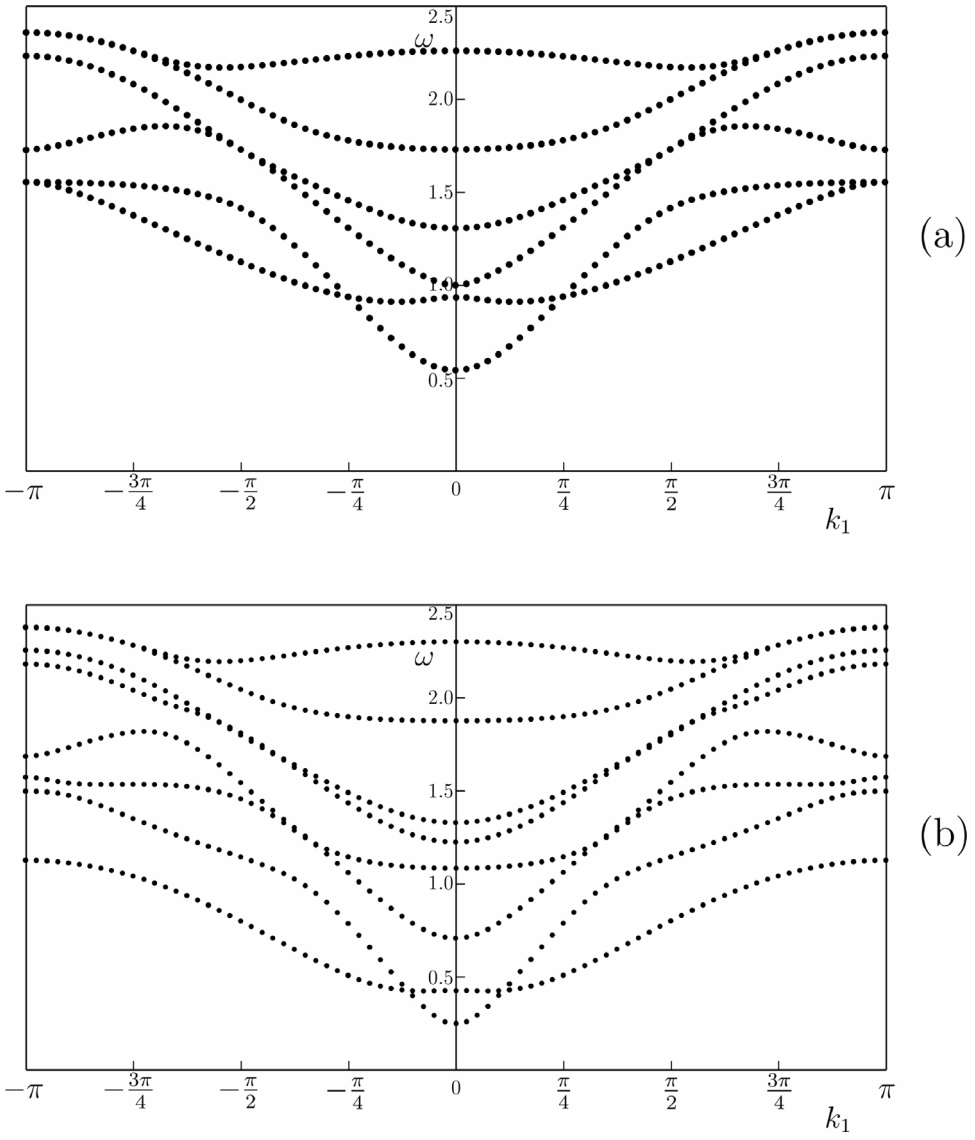

Fig. 7. Dispersion curves for the homogeneous triangular lattice with (a) clamped–clamped and (b) clamped–free boundary conditions. In both figures, $N = 4$.

$$\boldsymbol{B}_{\mathrm{CF}} = \begin{pmatrix} \boldsymbol{H}(\Lambda_1) & \boldsymbol{H}(\Lambda_2) & \boldsymbol{H}(\Lambda_1^{-1}) & \boldsymbol{H}(\Lambda_2^{-1}) \\ \Lambda_1^N \boldsymbol{B}_{\mathrm{U}}(\Lambda_1)\boldsymbol{H}(\Lambda_1) & \Lambda_2^N \boldsymbol{B}_{\mathrm{U}}(\Lambda_2)\boldsymbol{H}(\Lambda_2) & \Lambda_1^{-N} \boldsymbol{B}_{\mathrm{U}}(\Lambda_1^{-1})\boldsymbol{H}(\Lambda_1^{-1}) & \Lambda_2^{-N} \boldsymbol{B}_{\mathrm{U}}(\Lambda_2^{-1})\boldsymbol{H}(\Lambda_2^{-1}) \end{pmatrix} \tag{55}$$

Box II.

In this case, the homogeneous system has the form

$$\boldsymbol{B}_{\mathrm{CF}}\, \boldsymbol{C} = \boldsymbol{0}\,, \tag{54}$$

where $\boldsymbol{B}_{\mathrm{CF}}$ (Eq. (55)) is given in Box II with $\boldsymbol{B}_{\mathrm{U}}$ given in (20b).

The dispersion curves for clamped–free boundary conditions and $N = 4$ are shown in Fig. 7(b). In this case, the number of curves is equal to $2N$. A low-frequency stop-band is still present, but its size is smaller than that for the lattice with clamped–clamped boundary conditions, reported in part (a) of the same figure. Comparing the dispersion curves in Fig. 6(b), corresponding to a lattice with $N = 8$ and free–free boundary conditions, and those in Fig. 7(b), we observe that some frequencies are coincident. These frequencies are associated with eigenmodes of the lattice with $N = 8$ that have zero displacements at the nodes positioned in the central row ($n = N/2 = 4$).

3. Diatomic triangular lattice

In this section, we consider a triangular lattice with two types of particles, having masses M and μM, arranged as in a laminated strip (see Fig. 8). The length and the stiffness of each link are equal to L and Γ, respectively, as in Section 2. Free–free boundary conditions are assumed throughout this section. The displacement vectors associated with masses M and μM are denoted by $\boldsymbol{u}$ and $\boldsymbol{v}$, respectively. As for the monatomic lattice analysed in Section 2, we assume that N is an even number.

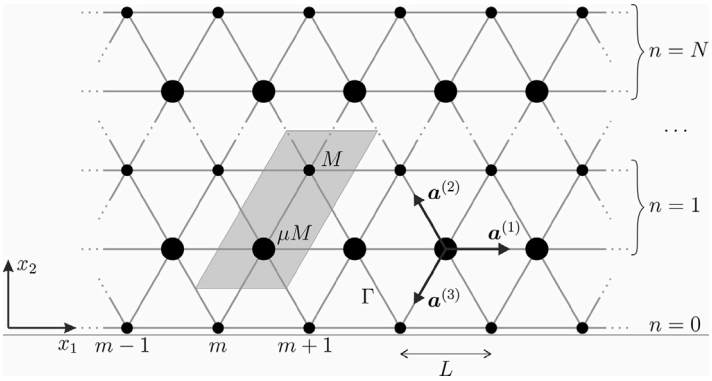

Fig. 8. Two-dimensional periodic lattice strip, consisting of two types of particles. Free–free boundary conditions are considered. The elementary cell of the system is highlighted in grey colour.

3.1. Eigensolutions for Lamb waves in the diatomic lattice

Following a similar procedure presented above for the monoatomic lattice, in the following we determine the eigensolutions for the time-harmonic problem, starting from the governing equations in the bulk and obtaining the relative eigensolutions by imposing the boundary conditions.

3.1.1. Equations for the diatomic lattice's bulk

The governing equations for the particles belonging to the interior of the diatomic lattice ($0 < n < N$) are expressed by

$$\begin{aligned} M\ddot{\boldsymbol{u}}^{(m,n)} = \; & \Gamma\left[\boldsymbol{a}^{(1)}\cdot\left(\boldsymbol{u}^{(m+1,n)}+\boldsymbol{u}^{(m-1,n)}-2\boldsymbol{u}^{(m,n)}\right)\boldsymbol{a}^{(1)}\right. \\ & +\boldsymbol{a}^{(2)}\cdot\left(\boldsymbol{v}^{(m-1,n+1)}+\boldsymbol{v}^{(m+1,n)}-2\boldsymbol{u}^{(m,n)}\right)\boldsymbol{a}^{(2)} \\ & \left.+\;\boldsymbol{a}^{(3)}\cdot\left(\boldsymbol{v}^{(m,n+1)}+\boldsymbol{v}^{(m,n)}-2\boldsymbol{u}^{(m,n)}\right)\boldsymbol{a}^{(3)}\right], \end{aligned} \tag{56a}$$

$$\begin{aligned} \mu M\ddot{\boldsymbol{v}}^{(m,n)} = \; & \Gamma\left[\boldsymbol{a}^{(1)}\cdot\left(\boldsymbol{v}^{(m+1,n)}+\boldsymbol{v}^{(m-1,n)}-2\boldsymbol{v}^{(m,n)}\right)\boldsymbol{a}^{(1)}\right. \\ & +\boldsymbol{a}^{(2)}\cdot\left(\boldsymbol{u}^{(m-1,n)}+\boldsymbol{u}^{(m+1,n-1)}-2\boldsymbol{v}^{(m,n)}\right)\boldsymbol{a}^{(2)} \\ & \left.+\;\boldsymbol{a}^{(3)}\cdot\left(\boldsymbol{u}^{(m,n)}+\boldsymbol{u}^{(m,n-1)}-2\boldsymbol{v}^{(m,n)}\right)\boldsymbol{a}^{(3)}\right], \end{aligned} \tag{56b}$$

where the vectors $\boldsymbol{a}^{(j)}$ ($j = 1,2,3$) are given in (2) (see also Fig. 8).

Normalising the equations above as in Eq. (4) and considering time-harmonic conditions (refer to (3)), with the addition $\boldsymbol{v} = L\tilde{\boldsymbol{v}}$ and $\boldsymbol{V} = L\tilde{\boldsymbol{V}}$ we obtain:

$$\begin{aligned} \omega^2\boldsymbol{U}^{(m,n)} \; & +\boldsymbol{a}^{(1)}\cdot\left(\boldsymbol{U}^{(m+1,n)}+\boldsymbol{U}^{(m-1,n)}-2\boldsymbol{U}^{(m,n)}\right)\boldsymbol{a}^{(1)} \\ & +\boldsymbol{a}^{(2)}\cdot\left(\boldsymbol{V}^{(m-1,n+1)}+\boldsymbol{V}^{(m+1,n)}-2\boldsymbol{U}^{(m,n)}\right)\boldsymbol{a}^{(2)} \\ & +\boldsymbol{a}^{(3)}\cdot\left(\boldsymbol{V}^{(m,n+1)}+\boldsymbol{V}^{(m,n)}-2\boldsymbol{U}^{(m,n)}\right)\boldsymbol{a}^{(3)}=\boldsymbol{0}, \end{aligned} \tag{57a}$$

$$\begin{aligned} \mu\omega^2\boldsymbol{V}^{(m,n)} \; & +\boldsymbol{a}^{(1)}\cdot\left(\boldsymbol{V}^{(m+1,n)}+\boldsymbol{V}^{(m-1,n)}-2\boldsymbol{V}^{(m,n)}\right)\boldsymbol{a}^{(1)} \\ & +\boldsymbol{a}^{(2)}\cdot\left(\boldsymbol{U}^{(m-1,n)}+\boldsymbol{U}^{(m+1,n-1)}-2\boldsymbol{V}^{(m,n)}\right)\boldsymbol{a}^{(2)} \\ & +\boldsymbol{a}^{(3)}\cdot\left(\boldsymbol{U}^{(m,n)}+\boldsymbol{U}^{(m,n-1)}-2\boldsymbol{V}^{(m,n)}\right)\boldsymbol{a}^{(3)}=\boldsymbol{0}, \end{aligned} \tag{57b}$$

where $\boldsymbol{U}$ and $\boldsymbol{V}$ are the displacement amplitude vectors. Note that, as before, we avoid the tilde atop of the dimensionless variables for ease of notation.

Employing the ansatz

$$\boldsymbol{U}^{(m,n)} = \Lambda^n\boldsymbol{H}\mathrm{e}^{-\mathrm{i}k_1(m+n)}, \tag{58a}$$

$$\boldsymbol{V}^{(m,n)} = \Lambda^n\boldsymbol{L}\mathrm{e}^{-\mathrm{i}k_1(m+n)}, \tag{58b}$$

with $\boldsymbol{H} = (H_1, H_2)^T$ and $\boldsymbol{L} = (L_1, L_2)^T$, and following algebraic simplifications, the system (57) takes the form

$$\boldsymbol{S}\,\boldsymbol{J} = \boldsymbol{0}, \tag{59}$$

where $\boldsymbol{S}$ (Eq. (60)) is given in Box III and $\boldsymbol{J} = (\boldsymbol{H}, \boldsymbol{L})^{\mathrm{T}}$.

The condition $\det(\boldsymbol{S}) = 0$ leads to a 4th-order equation in Λ, whose solutions are

$$\Lambda_{1,3} = \eta_a \pm \sqrt{\eta_a^2 - 1}, \tag{61a}$$

$$\Lambda_{2,4} = \eta_b \pm \sqrt{\eta_b^2 - 1}, \tag{61b}$$

where

$$\eta_{a,b} = p \pm \sqrt{p^2 - q} \tag{62}$$

and the coefficients p and q are in this case given by

$$\begin{aligned} p = \; & \frac{1}{18}\left\{-18+4\mu\omega^4+(4\omega^2-9)(4\mu\omega^2-9)\cos(k_1)\right. \\ & \left.+6\left[2(1+\mu)\omega^2-9\right]\cos(2k_1)+9\cos(3k_1)\right\}, \end{aligned} \tag{63a}$$

$$\begin{aligned} q = \; & \frac{1}{18}\left\{549-396(1+\mu)\omega^2+8\left[9+\mu(34+9\mu)\right]\omega^4-48\mu(1+\mu)\omega^6\right. \\ & +8\mu^2\omega^8 \\ & +2\left[-351+204(1+\mu)\omega^2-4(6+25\mu+6\mu^2)\omega^4+8\mu(1+\mu)\omega^6\right] \\ & \times\cos(k_1) \\ & \left.+\left[189-60(1+\mu)\omega^2+16\mu\omega^4\right]\cos(2k_1)-18\cos(3k_1)\right\}. \end{aligned} \tag{63b}$$

We note that $\Lambda_3 = \Lambda_1^{-1}$ and $\Lambda_4 = \Lambda_2^{-1}$.

Accordingly, the displacement amplitude vectors can be written as

$$\begin{aligned} \boldsymbol{U}^{(m,n)} = \; & \left[C_1\Lambda_1^n\boldsymbol{H}(\Lambda_1)+C_2\Lambda_2^n\boldsymbol{H}(\Lambda_2)+C_3\Lambda_1^{-n}\boldsymbol{H}(\Lambda_1^{-1})\right. \\ & \left.+C_4\Lambda_2^{-n}\boldsymbol{H}(\Lambda_2^{-1})\right]\mathrm{e}^{-\mathrm{i}k_1(m+n)}, \end{aligned} \tag{64a}$$

$$\begin{aligned} \boldsymbol{V}^{(m,n)} = \; & \left[C_1\Lambda_1^n\boldsymbol{L}(\Lambda_1)+C_2\Lambda_2^n\boldsymbol{L}(\Lambda_2)+C_3\Lambda_1^{-n}\boldsymbol{L}(\Lambda_1^{-1})\right. \\ & \left.+C_4\Lambda_2^{-n}\boldsymbol{L}(\Lambda_2^{-1})\right]\mathrm{e}^{-\mathrm{i}k_1(m+n)}, \end{aligned} \tag{64b}$$

where C_j ($j = 1,\dots,4$) are unknown coefficients. We can take $\boldsymbol{H} = (1, h_2)^{\mathrm{T}}$ and $\boldsymbol{L} = (l_1, l_2)^{\mathrm{T}}$, where the components h_2, l_1 and l_2 are determined from the system (59) as:

$$\begin{aligned} h_2(\Lambda) &= -\frac{\sqrt{3}}{4}\frac{(\Lambda-1)(e^{-ik_1}-1)}{\omega^2-3}l_1(\Lambda)-\frac{3}{4}\frac{(\Lambda+1)(e^{-ik_1}+1)}{\omega^2-3}l_2(\Lambda), \\ l_1(\Lambda) &= -\frac{3\sqrt{3}\mathrm{i}}{8}\frac{(\Lambda-\Lambda^{-1})\sin(k_1)}{\xi(\Lambda)}l_2(\Lambda)-\frac{1}{4}\frac{(\omega^2-3)(\Lambda^{-1}+1)(e^{ik_1}+1)}{\xi(\Lambda)}, \\ l_2(\Lambda) &= \frac{2\sqrt{3}(\omega^2-3)\{3\mathrm{i}(\Lambda^{-1}+1)(\Lambda-\Lambda^{-1})(e^{ik_1}+1)\sin(k_1)-8(\Lambda^{-1}-1)\,\xi(\Lambda)(e^{ik_1}-1)\}}{64\{(\omega^2-3)(\mu\omega^2-3)-\frac{9}{4}(\Lambda+\Lambda^{-1}+2)\cos^2(k_1/2)\}\,\xi(\Lambda)+27\sin^2(k_1)(\Lambda-\Lambda^{-1})^2}, \end{aligned} \tag{65}$$

with

$$\xi(\Lambda) = (\omega^2-3)(\mu\omega^2+2\cos(k_1)-3)-\frac{3}{4}(2-\Lambda-\Lambda^{-1})\sin^2(k_1/2). \tag{66}$$

3.1.2. Conditions for the diatomic lattice's free boundaries

Following the procedure outlined in Section 2.3, at the lattice's free boundaries, we obtain that the following conditions hold:

$$\begin{aligned} & \boldsymbol{a}^{(2)}\cdot\left(\boldsymbol{V}^{(m+1,0)}-\boldsymbol{U}^{(m,0)}\right)\boldsymbol{a}^{(2)} \\ & +\boldsymbol{a}^{(3)}\cdot\left(\boldsymbol{V}^{(m,0)}-\boldsymbol{U}^{(m,0)}\right)\boldsymbol{a}^{(3)}=\boldsymbol{0} \qquad \text{for } n=0, \end{aligned} \tag{67a}$$

$$\begin{aligned} & \boldsymbol{a}^{(2)}\cdot\left(\boldsymbol{V}^{(m-1,N+1)}-\boldsymbol{U}^{(m,N)}\right)\boldsymbol{a}^{(2)} \\ & +\boldsymbol{a}^{(3)}\cdot\left(\boldsymbol{V}^{(m,N+1)}-\boldsymbol{U}^{(m,N)}\right)\boldsymbol{a}^{(3)}=\boldsymbol{0} \qquad \text{for } n=N. \end{aligned} \tag{67b}$$

$$\boldsymbol{S} = \begin{pmatrix} \omega^2 + 2\cos(k_1) - 3 & 0 & \frac{1}{4}(\Lambda+1)(\mathrm{e}^{-\mathrm{i}k_1}+1) & \frac{\sqrt{3}}{4}(\Lambda-1)(\mathrm{e}^{-\mathrm{i}k_1}-1) \\ 0 & \omega^2 - 3 & \frac{\sqrt{3}}{4}(\Lambda-1)(\mathrm{e}^{-\mathrm{i}k_1}-1) & \frac{3}{4}(\Lambda+1)(\mathrm{e}^{-\mathrm{i}k_1}+1) \\ \frac{1}{4}(\Lambda^{-1}+1)(\mathrm{e}^{\mathrm{i}k_1}+1) & \frac{\sqrt{3}}{4}(\Lambda^{-1}-1)(\mathrm{e}^{\mathrm{i}k_1}-1) & \mu\omega^2 + 2\cos(k_1) - 3 & 0 \\ \frac{\sqrt{3}}{4}(\Lambda^{-1}-1)(\mathrm{e}^{\mathrm{i}k_1}-1) & \frac{3}{4}(\Lambda^{-1}+1)(\mathrm{e}^{\mathrm{i}k_1}+1) & 0 & \mu\omega^2 - 3 \end{pmatrix} \tag{60}$$

Box III.

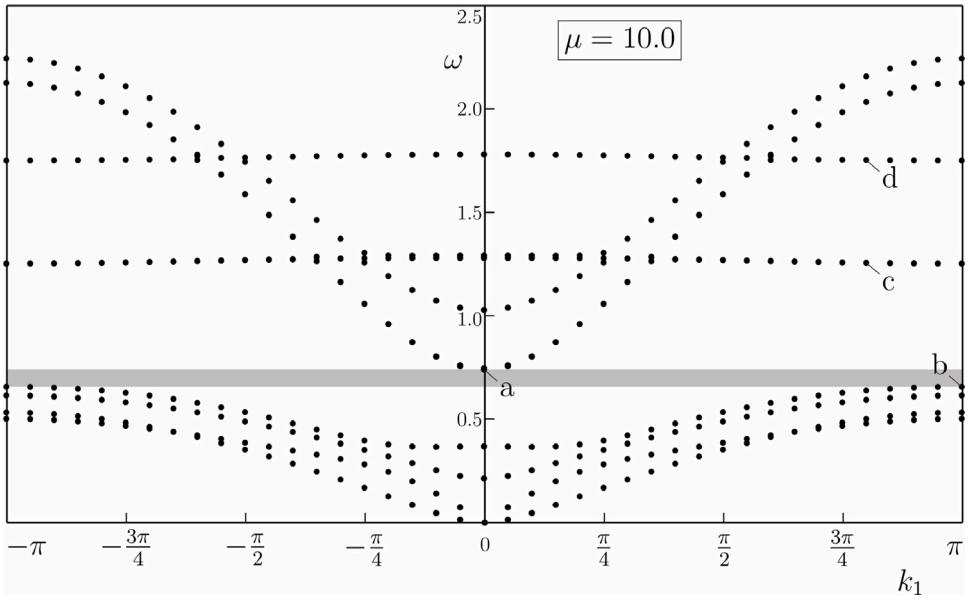

Fig. 9. Dispersion curves for the diatomic lattice sketched in Fig. 8, having five rows and free–free boundary conditions. Here, the mass ratio is $\mu = 10.0$.

After algebraic manipulations, we arrive at the homogeneous system

$$\boldsymbol{T}_{\mathrm{FF}}\,\boldsymbol{C} = \boldsymbol{0}\,, \tag{68}$$

where the vector of unknowns is $\boldsymbol{C} = \left(C_1, C_2, C_3, C_4\right)^{\mathrm{T}}$ and the coefficients matrix is given by

$$\boldsymbol{T}_{\mathrm{FF}} = \begin{pmatrix} \boldsymbol{T}_{\mathrm{L}}\boldsymbol{J}(\Lambda_1) & \boldsymbol{T}_{\mathrm{L}}\boldsymbol{J}(\Lambda_2) & \boldsymbol{T}_{\mathrm{L}}\boldsymbol{J}(\Lambda_1^{-1}) & \boldsymbol{T}_{\mathrm{L}}\boldsymbol{J}(\Lambda_2^{-1}) \\ \Lambda_1^N\boldsymbol{T}_{\mathrm{U}}(\Lambda_1)\boldsymbol{J}(\Lambda_1) & \Lambda_2^N\boldsymbol{T}_{\mathrm{U}}(\Lambda_2)\boldsymbol{J}(\Lambda_2) & \Lambda_1^{-N}\boldsymbol{T}_{\mathrm{U}}(\Lambda_1^{-1})\boldsymbol{J}(\Lambda_1^{-1}) & \Lambda_2^{-N}\boldsymbol{T}_{\mathrm{U}}(\Lambda_2^{-1})\boldsymbol{J}(\Lambda_2^{-1}) \end{pmatrix}. \tag{69}$$

Here, $\boldsymbol{J} = \left(1, h_2, l_1, l_2\right)^{\mathrm{T}}$,

$$\boldsymbol{T}_{\mathrm{L}} = \begin{pmatrix} -2 & 0 & 1+\mathrm{e}^{-\mathrm{i}k_1} & \sqrt{3}\left(1-\mathrm{e}^{-\mathrm{i}k_1}\right) \\ 0 & -2\sqrt{3} & 1-\mathrm{e}^{-\mathrm{i}k_1} & \sqrt{3}\left(1+\mathrm{e}^{-\mathrm{i}k_1}\right) \end{pmatrix}, \tag{70a}$$

$$\boldsymbol{T}_{\mathrm{U}}(\Lambda_j) = \begin{pmatrix} -2 & 0 & \left(\mathrm{e}^{-\mathrm{i}k_1}+1\right)\Lambda_j & \sqrt{3}\left(\mathrm{e}^{-\mathrm{i}k_1}-1\right)\Lambda_j \\ 0 & -2\sqrt{3} & \left(\mathrm{e}^{-\mathrm{i}k_1}-1\right)\Lambda_j & \sqrt{3}\left(\mathrm{e}^{-\mathrm{i}k_1}+1\right)\Lambda_j \end{pmatrix}. \tag{70b}$$

3.2. Dispersion diagrams

Imposing $\det\left(\boldsymbol{T}_{\mathrm{FF}}\right) = 0$, we derive several solutions for the radian frequency ω as functions of the wavenumber k_1, which represent the dispersion curves for the diatomic lattice with free–free boundary conditions. The dispersion diagram for a mass ratio $\mu = 10.0$ and five rows ($N = 2$) is shown in Fig. 9.

The number of dispersion curves is twice the number of rows, as for the monatomic lattice studied in Section 2. Differently from the latter, the dispersion diagram in Fig. 9 contains an internal stop-band, whose width can be expanded by increasing the mass ratio μ. In addition, we notice the presence of two pairs of flat bands, each pair being characterised by two nearly coincident curves.

3.2.1. Eigenmodes

Here, we describe interesting modes of vibrations, evaluated at some important points of the dispersion diagram.

We start from investigating the limits of the internal band-gap. The eigenmode determined at $(k_1, \omega) = (0, 0.738)$, indicated by "a" in Fig. 9, is illustrated in Video2(a) of the Supplementary Material. At this particular value of the frequency and wavenumber, the vibrations are mainly confined in the rows where the smaller masses are positioned; moreover, the particles move only in the horizontal direction. On the other hand, in the lower limit of the internal stop-band where $(k_1, \omega) = (\pi, 0.656)$ (point "b" in Fig. 9), the eigenmode is such that the nodal points in the central row ($n = 2$) remain almost fixed, while in the other rows the small (big) masses displace vertically (horizontally) (see Video2(b)).

Next, we examine the vibrations at some frequencies belonging to the flat bands. In the lower one (see point "c" in Fig. 9), where $(k_1, \omega) = (4\pi/5, 1.25)$ the small masses at the boundaries move in the vertical direction, while all the particles in the other three rows undergo displacements of relative negligible amplitude (see Video2(c)). Conversely, in the upper flat band (in particular at point "d", where $(k_1, \omega) = (4\pi/5, 1.75)$) the vibrations are mainly confined in the central row, where the particles move again in the vertical direction (see Video2(d)).

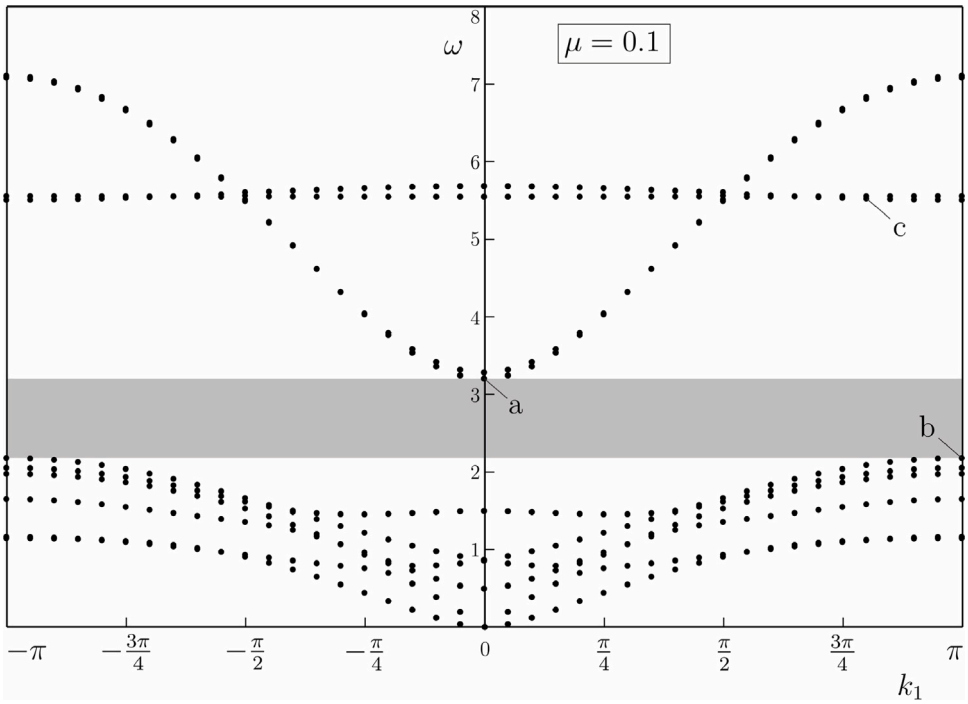

Fig. 10. Same as in Fig. 9, but for a mass ratio equal to $\mu = 0.1$.

3.2.2. Lattice with $\mu < 1$

In order to better understand the dynamic features of the diatomic lattice, we consider a discrete system where bigger and smaller masses are swapped with respect to the scenario shown in Fig. 8. In particular, we take $\mu = 0.1$, which is the reciprocal value of the mass ratio considered in the previous sections.

The dispersion curves for this value of the mass ratio are shown in Fig. 10. We notice that the frequencies are larger than those in Fig. 9, because the total mass of the particles within the elementary cell is smaller. An internal stop-band still appears, due to the high contrast of the masses of the diatomic lattice.

It is interesting to look at the eigenmodes for $\mu = 0.1$ and compare them with those calculated for $\mu = 10.0$, discussed in Section 3.2.1. In the upper limit of the internal stop-band (point "a" in Fig. 10, corresponding to $(k_1, \omega) = (0, 3.203)$), vibrations are confined in the rows where smaller masses are located and the motion occurs in the horizontal direction (see Video3(a)); this is analogous to what observed for $\mu = 10.0$ (see Video2(a)). In the lower limit of the internal stop-band (point "b" in Fig. 10, where $(k_1, \omega) = (\pi, 2.176)$) bigger masses vibrate horizontally, while smaller masses move vertically (see Video3(b)), as for $\mu = 10.0$ (see Video2(b)). In the flat band (see, for example, point "c" in Fig. 10, whose coordinates are $(k_1, \omega) = (4\pi/5, 5.52)$), only smaller masses move significantly and their trajectories are in the vertical direction (see Video3(c)), in agreement with what found for $\mu = 10.0$ (see Video2(c) and Video2(d)). In the present case, however, there is only one flat band, because there are no other rows with smaller masses (on the other hand, for $\mu = 10.0$ there are two flat bands because motion can be localised in either the boundary rows or in the central row, where smaller masses are).

We note that, in both cases $\mu \gtrless 1$, the above mentioned eigenmodes display remarkable behaviours since the trajectories of nodes are unidirectional in contrast with the motions of the boundary points for the classical solutions of both Lamb and Rayleigh waves in a continuum or discrete solid; in such cases the trajectories are ellipsoidal. A similar property can be obtained, both in continuum and discrete solids with the introduction of a gyroscopic effect, as shown by Nieves et al. (2020).

3.2.3. Dependence of the dispersion properties on the mass ratio μ

The presence of an internal band-gap in the dispersion diagram clearly depends on the mass ratio μ. In particular, we have noticed that, for $\mu \geq 1$, the internal band-gap appears when the fifth frequency at $k_1 = 0$ becomes larger than the fourth frequency at $k_1 = \pi$. Therefore, we have performed a parametric analysis, where we have calculated the radian frequencies at $k_1 = 0$ and $k_1 = \pi$ for $1 \leq \mu \leq 15$. The results are shown in Fig. 11. The region coloured in grey represents the internal band-gap, which appears when $\mu > 7.519$.

The evolution of the dispersion diagram for increasing values of the mass ratio is shown in Fig. 12. In particular, three values of the mass ratio have been considered: $\mu = 2.5, 5.0, 7.519$ (we recall that the dispersion curves for $\mu = 10.0$ have been reported in Fig. 9). We note that for small values of μ (e.g., $\mu = 2.5$ in part (a)) the maximum of the fourth dispersion curve is not found at $k_1 = \pi$. However, for $\mu > 5.0$, for which an internal stop-band has not appeared yet (see part (b)), the maximum of the fourth dispersion curve is located at $k_1 = \pi$. For $\mu = 7.519$, the fourth frequency at $k_1 = \pi$ coincides with the fifth frequency at $k_1 = 0$ (see part (c)). Hence, when $\mu > 7.519$ an internal band-gap appears and its width increases as the mass ratio μ becomes larger.

4. Application: one-way wave propagation in discrete strips

In this section, we show how mode conversion and selection can be exploited to force waves to travel in a single direction (Zhu et al., 2010).

To this aim, we consider two periodic lattices made of two types of masses, whose ratio is denoted by μ as in Section 3. The unit cells of the two periodic diatomic lattices are sketched in the insets on the bottom part of Fig. 13. We note that the width of these unit cells is twice the width of the periodic cells in Figs. 2 and 8. In part (a) (part (b)) of Fig. 13 an antisymmetric (symmetric) lattice is analysed. The corresponding dispersion curves, obtained numerically, are reported on the top diagrams of Fig. 13 in the range $0 \leq \omega \leq 1.6$.

The dispersion curves for the antisymmetric lattice in Fig. 13(a) are associated with hybrid modes, represented as combinations of symmetric and antisymmetric modes. Conversely, the symmetric lattice

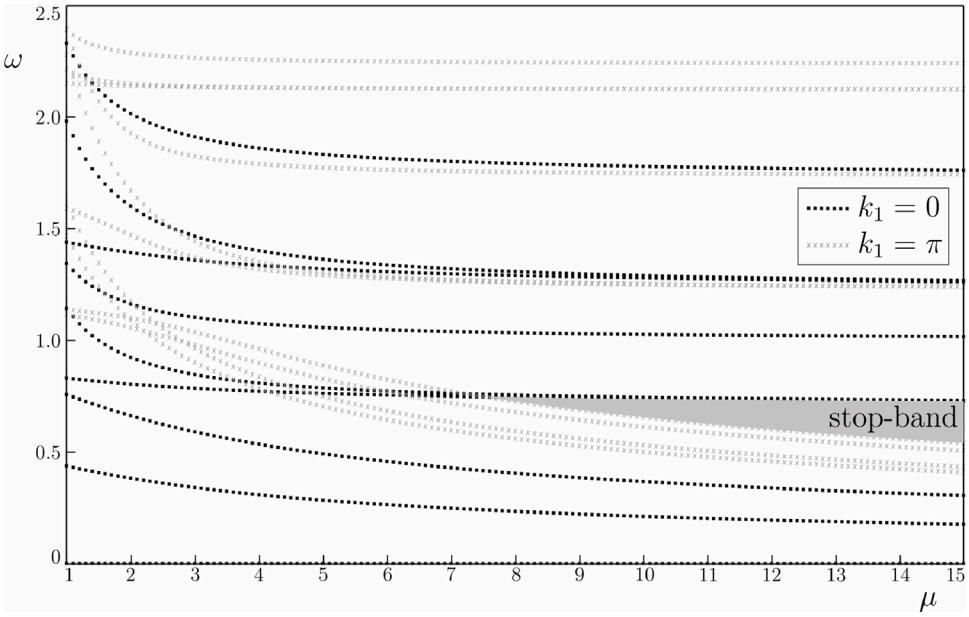

Fig. 11. Radian frequencies ω evaluated at $k_1 = 0$ (black dots) and $k_1 = \pi$ (grey crosses), as functions of the mass ratio μ.

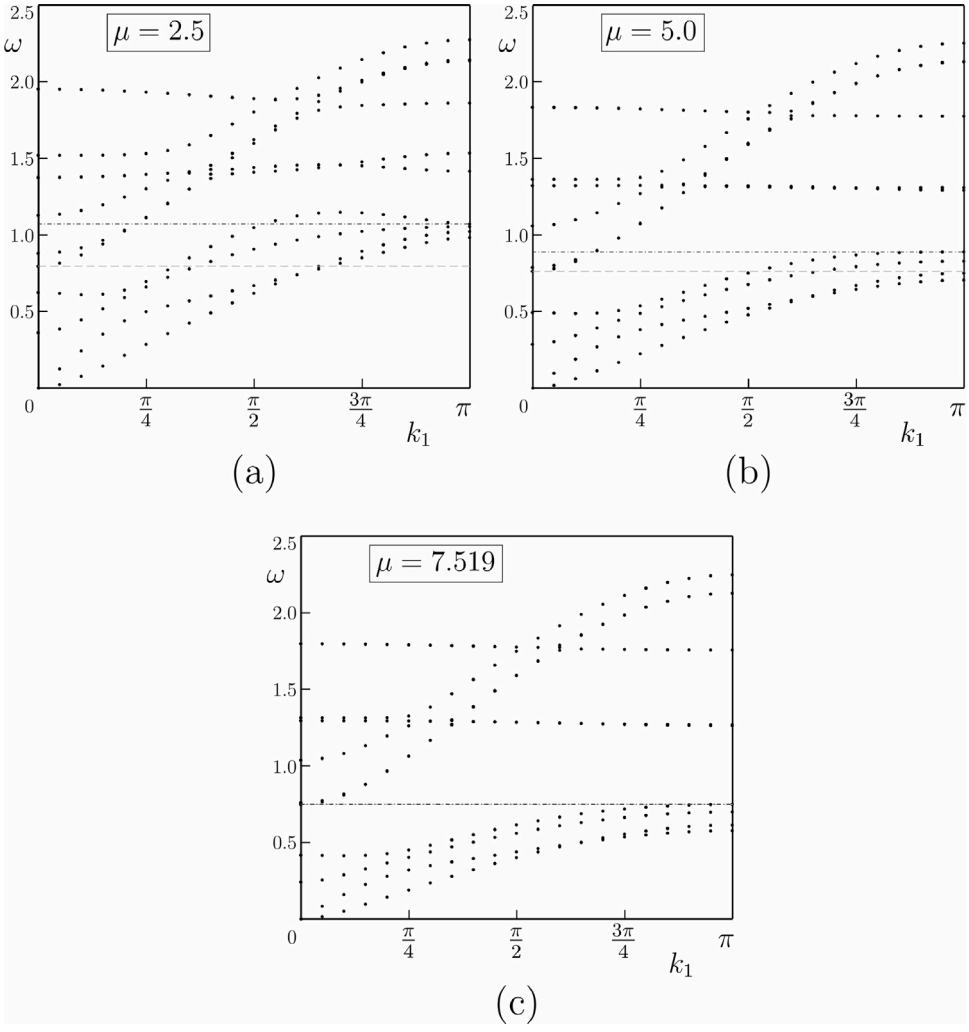

Fig. 12. Dispersion curves calculated for the diatomic lattice with $N = 2$, free–free boundary conditions and (a) $\mu = 2.5$, (b) $\mu = 5.0$, (c) $\mu = 7.519$. The horizontal dot–dashed and dashed lines represent the fourth and fifth frequencies computed at $k_1 = \pi$ and $k_1 = 0$, respectively.

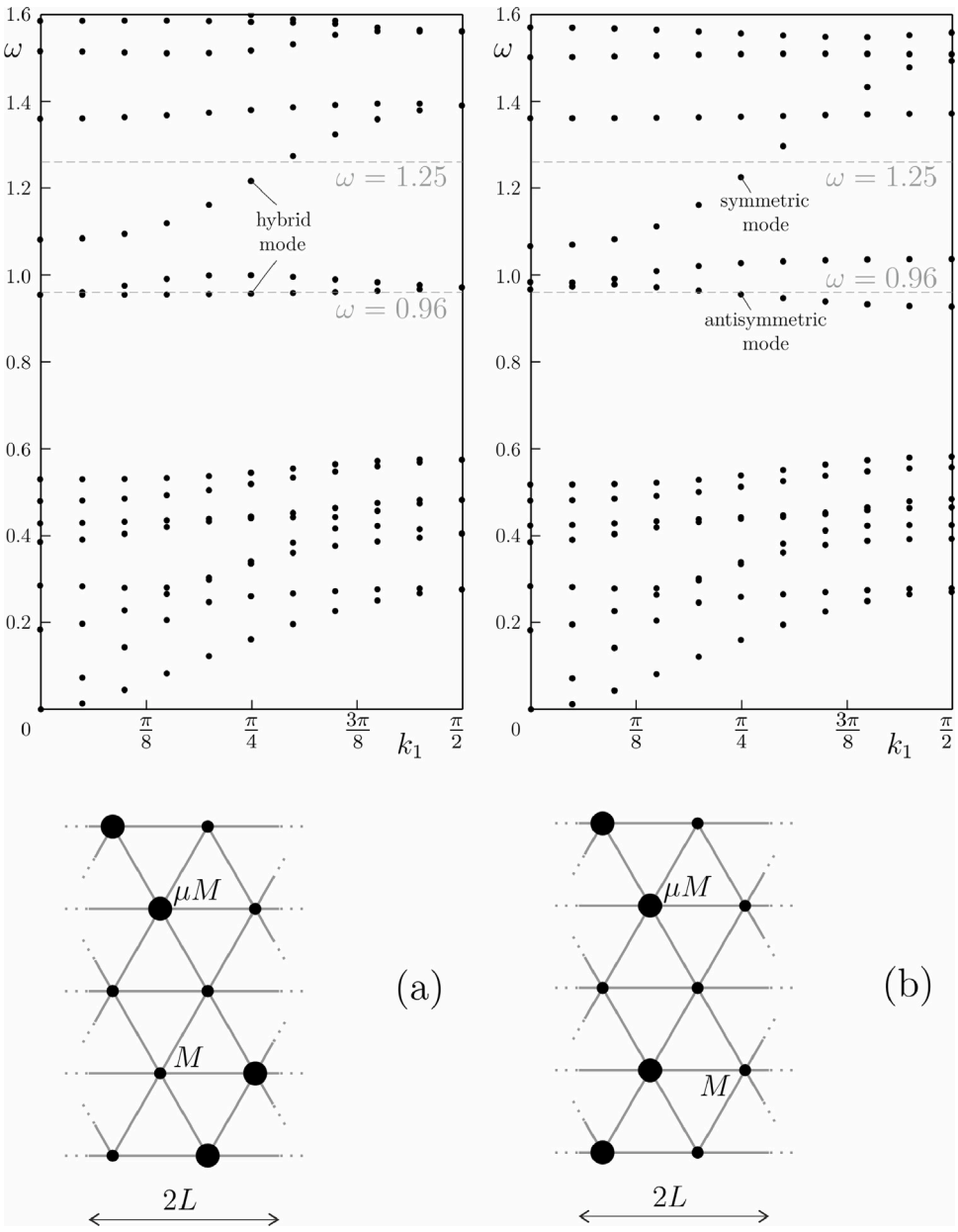

Fig. 13. Dispersion curves (top) corresponding to the periodic unit cells (bottom) for the (a) antisymmetric and (b) symmetric lattices. The ratio between bigger and smaller masses is given by $\mu = 10.0$. The horizontal dashed lines in the dispersion diagrams indicate the frequencies of the time-harmonic loads considered in the forced problems, discussed in the following.

in Fig. 13(b) is characterised by either symmetric or antisymmetric modes.

Now we consider a finite structure made of an anti-symmetric and a symmetric lattice joined together, as shown in Fig. 14(a) and (c). The interface between the two lattices is represented by a dashed line. PML (Perfectly Matched Layers) are introduced near the ends of the strip to avoid wave reflection at the left and right boundaries. In part (a), an antisymmetric time-harmonic load is applied at the left of the structure. Its frequency is given by $\omega = 1.25$. Referring to Fig. 13, this frequency intersects a hybrid mode in the antisymmetric lattice (part (a)) and a symmetric mode in the symmetric lattice (part (b)). Therefore, the wave generated by the antisymmetric load becomes hybrid when travelling through the antisymmetric lattice; when it reaches the symmetric lattice, only the symmetric component propagates. Consequently, the wave is allowed to propagate in the forward direction (from the left to the right of the strip), as shown in part (b).

On the other hand, in part (c) the same load is applied near the right end of the strip. Being antisymmetric, it cannot propagate through the symmetric lattice since that frequency corresponds to a symmetric mode. Hence, the wave is localised near the point of application of the load and cannot propagate in the backward direction (namely from the right to the left), as demonstrated by the response of the system reported in part (d). Using mode conversion and selection, we have designed a discrete strip which sustains one-way wave propagation, in the same spirit as the continuous phononic crystals presented in Zhu et al. (2010).

A similar behaviour can be obtained by imposing a symmetric load. In this case, we need to choose a frequency that intersects a hybrid mode in the antisymmetric lattice and an antisymmetric mode in the symmetric one. In particular, we take $\omega = 0.96$ (refer to Fig. 13). When the symmetric load is applied at the left of the strip (see Fig. 15(a)), it excites a hybrid mode so that the ensuing wave propagates through

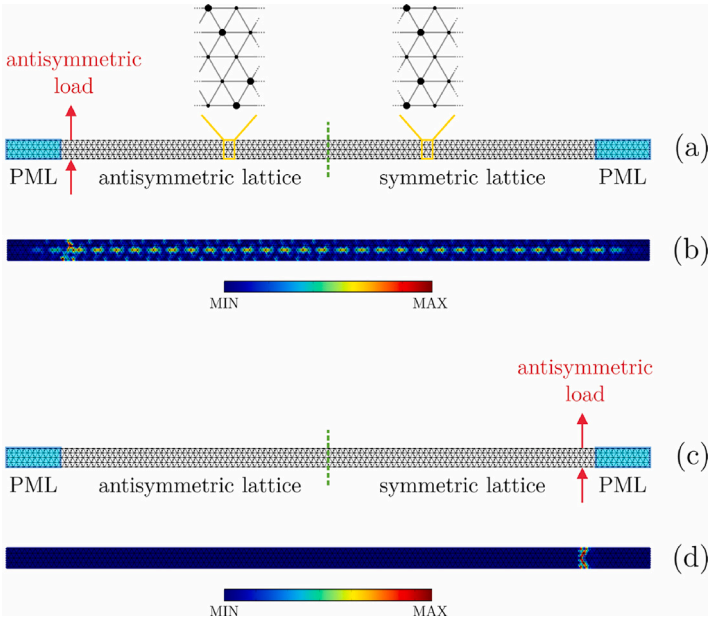

Fig. 14. (a,c) Structure made of an antisymmetric lattice (left) and a symmetric lattice (right), whose unit cells are detailed in (a). An antisymmetric time-harmonic load of frequency $\omega = 1.25$ is imposed at the (a) left and (c) right of the strip, as indicated by the arrows. PML are inserted in proximity of the ends of the structure. (b,d) Displacement fields resulting from the loading conditions in (a,c), respectively.

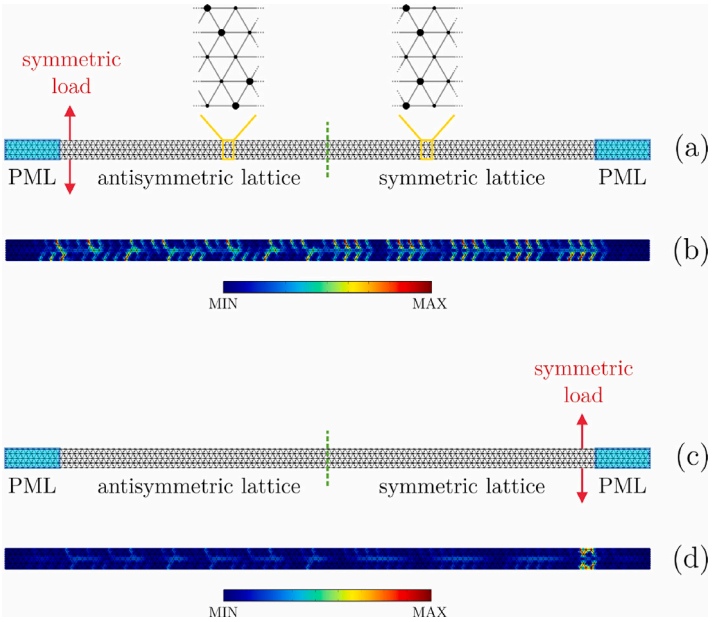

Fig. 15. Same finite structure as in Fig. 14, but considering a symmetric load having frequency $\omega = 0.96$.

the antisymmetric lattice. When it reaches the interface, only the antisymmetric part travels through the symmetric lattice, reaching the right end of the strip (see Fig. 15(b)). Conversely, when the symmetric load is imposed near the right end of the finite structure (see Fig. 15(c)), it cannot travel through the symmetric lattice because at that frequency only antisymmetric modes can be activated. As a consequence, the wave remains confined near the application point of the load (see Fig. 15(d)).

5. Conclusions

We have studied the dispersion features of Lamb waves in both monatomic and diatomic lattice strips. For both cases, we have derived analytically the dispersion equations.

For monatomic lattices, we have shown how to characterise symmetric and antisymmetric eigenmodes, identifying them in the dispersion diagram. In addition, we have found that the number of dispersion curves is a linear function of the number of rows within the strip and that it also depends on the imposed conditions at the boundaries. In particular, we have considered free–free, clamped–clamped and clamped–free boundary conditions. In the low-frequency long-wave limit, we have obtained agreement with the continuum beam equations, describing the motion of longitudinal and flexural waves.

Regarding the diatomic lattice, we have proved the existence of an internal band-gap, that appears for large values of the ratio between the masses of the two types of particles. Moreover, we have observed the presence of flat bands in the dispersion diagram, corresponding to

resonant modes. The analysis of the eigenmodes, evaluated at specific values of the frequency, has helped us detect interesting modes of vibrations of the microstructured strip, which evidence unidirectional polarisations.

In addition, we have investigated asymptotically some natural limiting cases of the considered discrete elastic medium. This includes the case when the number of rows of the strip become infinite, where we have shown that the Rayleigh wave problem for an elastic lattice half-space is encountered. Further, we have demonstrated numerically that, for large N, the dispersive features of a strip with a finite width and a dense internal microstructure can reproduce the dispersive nature of a continuum elastic strip of the same width.

The developed theory has led to the design of a discrete heterogeneous elastic system capable of selecting waves of a specific type from wave packets generated by an applied load and propagating only these particular waves in a single direction in the structure. Potential applications of this system include the design of novel Micro-Electro-Mechanical-System devices (MEMs) that can convey energy in selective directions.

The formulation and application presented in this work can be easily extended to more complex lattice systems, comprising links of different stiffness or flexural ligaments, defects and resonators. We believe that the analytical work developed in this paper can be useful for several engineering applications at different scales, including Lamb-wave-based damage identification techniques used to find and characterise flaws in tested specimens, the dynamics of carbon nanotubes, near-surface seismic surveying, as well as the design of acoustic and elastic waveguides.

Declaration of competing interest

The authors declare they have no competing interests.

Acknowledgements

M.J.N. gratefully acknowledges the support of the EU H2020 grant MSCA-RISE-2020-101008140-EffectFact.

Appendix A. Supplementary data

Supplementary material related to this article can be found online at https://doi.org/10.1016/j.euromechsol.2022.104695.

References

Aydin, Y., Erbas, B., Kaplunov, J., Prikazchikova, L., 2018. Asymptotic analysis of an anti-plane dynamic problem for a three-layered strongly inhomogeneous laminate. Math. Mech. Solids 25 (2), 3–16. http://dx.doi.org/10.1177/1081286518790804.

Ayzenberg-Stepanenko, M.V., Slepyan, L.I., 2008. Resonant-frequency primitive waveforms and star waves in lattices. J. Sound Vib. 313 (3-5), 812–821. http://dx.doi.org/10.1016/j.jsv.2007.11.047.

Bacigalupo, A., Lepidi, M., Gnecco, G., Vadalà, F., Gambarotta, L., 2019. Optimal design of the band structure for beam lattice metamaterials. Front. Mater. 6, 2. http://dx.doi.org/10.3389/fmats.2019.00002.

Brillouin, L., 1953. Wave Propagation in Periodic Structures. Electric Filters and Crystal Lattices, second ed. Dover Publication, Inc., New York.

Brun, M., Giaccu, G.F., Movchan, A.B., Movchan, N.V., 2011. Asymptotics of eigenfrequencies in the dynamic response of elongated multi-structures. Proc. R. Soc. Lond. Ser. A Math. Phys. Eng. Sci. 468 (2138), 378–394. http://dx.doi.org/10.1098/rspa.2012.0165.

Brun, M., Jones, I.S., Movchan, A.B., 2012. Vortex-type elastic structured media and dynamic shielding. Proc. R. Soc. Lond. Ser. A Math. Phys. Eng. Sci. 468 (2146), 3027–3046. http://dx.doi.org/10.1098/rspa.2012.0165.

Carta, G., Brun, M., Movchan, A.B., Movchan, N., Jones, I.S., 2014. Dispersion properties of vortex-type monatomic lattices. Int. J. Solids Struct. 51, 2213–2225. http://dx.doi.org/10.1016/j.ijsolstr.2014.02.026.

Carta, G., Jones, I.S., Brun, M., Movchan, N.V., Movchan, A.B., 2013. Crack propagation induced by thermal shocks in structured media. Int. J. Solids Struct. 50 (18), 2725–2736. http://dx.doi.org/10.1016/j.ijsolstr.2013.05.001.

Carta, G., Jones, I.S., Movchan, N.V., Movchan, A.B., 2019. Wave characterisation in a dynamic elastic lattice: Lattice flux and circulation. Phys. Mesomech. 22, 152–163. http://dx.doi.org/10.1134/S102995991902005X.

Carta, G., Jones, I., Movchan, N., Movchan, A., Nieves, M., 2017. 'Deflecting elastic prism' and unidirectional localisation for waves in chiral elastic systems. Sci. Rep. 7, 2213–2225. http://dx.doi.org/10.1038/s41598-017-00054-6.

Colquitt, D.J., Jones, I.S., Movchan, N.V., Movchan, A.B., McPhedran, R.C., 2012. Dynamic anisotropy and localization in elastic lattice systems. Waves Random Complex Media 22 (2), 143–159. http://dx.doi.org/10.1080/17455030.2011.633940.

Diamanti, K., Soutis, C., Hodgkinson, J.M., 2005. Lamb waves for the non-destructive inspection of monolithic and sandwich composite beams. Composites A 36 (2), 189–195. http://dx.doi.org/10.1016/j.compositesa.2004.06.013.

Fu, Y., Kaplunov, J., Prikazchikov, D., 2020. Reduced model for the surface dynamics of a generally anisotropic elastic half-space. Proc. R. Soc. Lond. Ser. A Math. Phys. Eng. Sci. 476, 20190590. http://dx.doi.org/10.1098/rspa.2019.0590.

Garau, M., Carta, G., Nieves, M.J., Jones, I.S., Movchan, N.V., Movchan, A.B., 2018. Interfacial waveforms in chiral lattices with gyroscopic spinners. Proc. R. Soc. A. 474, 20180132. http://dx.doi.org/10.1098/rspa.2018.0132.

Garau, M., Nieves, M.J., Carta, G., Brun, M., 2019. Transient response of a gyro-elastic structured medium: Unidirectional waveforms and cloaking. Int. J. Eng. Sci. 143, 115–141. http://dx.doi.org/10.1016/j.ijengsci.2019.05.007.

Graff, K.F., 1975. Wave Motion in Elastic Solids. Oxford University Press.

Grünsteidl, C.M., Veres, I.A., 2015. Experimental and numerical study of the excitability of zero group velocity lamb waves by laser-ultrasound. J. Acoust. Soc. Am. 138, 242–250. http://dx.doi.org/10.1121/1.4922701.

Kachanov, M., Sevostianov, I., 2018. Micromechanics of Materials, with Applications. Springer, Berlin, ISBN: 978-3-030-09429-4.

Kaplunov, J., Prikazchikov, D., Prikazchikov, L., 2017. Dispersion of elastic waves in a strongly inhomogeneous three-layered plate. Int. J. Solids Struct. 113–114, 169–179. http://dx.doi.org/10.1016/j.ijsolstr.2017.01.042.

Kaplunov, J., Prikazchikov, D., Sultanova, L., 2019. Rayleigh-type waves on a coated elastic half-space with a clamped surface. Proc. R. Soc. Lond. Ser. A Math. Phys. Eng. Sci. 377, 20190111. http://dx.doi.org/10.1098/rsta.2019.0111.

Kaplunov, J., Prikazchikova, L., Alkinidri, M., 2021. Antiplane shear of an asymmetric sandwich plate. Contin. Mech. Thermodyn. 33, 1247–1262. http://dx.doi.org/10.1007/s00161-021-00969-6.

Kunin, I.A., 1982. Elastic Media with Microstructure I. One-Dimensional Models. In: Solid-State Sciences, Vol. 26, Springer, Berlin, Heidelberg, New York.

Lee, C.H., Li, G., Jin, G., Liu, Y., Zhang, X., 2018. Topological dynamics of gyroscopic and floquet lattices from Newton's laws. Phys. Rev. B 97, 085110. http://dx.doi.org/10.1103/PhysRevB.97.085110.

Marder, M., Gross, S., 1995. Origin of crack tip instabilities. J. Mech. Phys. Solids 43, 1–48. http://dx.doi.org/10.1016/0022-5096(94)00060-I.

Martinsson, P.G., Movchan, A.B., 2003. Vibrations of lattice structures and phononic band gaps. Q. J. Mech. Appl. Math. 56 (1), 45–64. http://dx.doi.org/10.1093/qjmam/56.1.45.

McPhedran, R.C., Movchan, A.B., Movchan, N.V., Brun, M., Smith, M.J.A., 2015. 'Parabolic' trapped modes and steered Dirac cones in platonic crystals. Proc. R. Soc. Lond. Ser. A Math. Phys. Eng. Sci. 471 (2177), 20140746. http://dx.doi.org/10.1098/rspa.2014.0746.

Mishuris, G.S., Movchan, A.B., Bigoni, D., 2012. Dynamics of a fault steadily propagating within a structural interface. Multiscale Model. Simul. 10 (3), 936–953. http://dx.doi.org/10.1137/110845732.

Mishuris, G.S., Movchan, N.V., Movchan, A.B., 2010. Dynamic mode-III interface crack in a bi-material strip. Int. J. Fract. 166, 121–133. http://dx.doi.org/10.1007/s10704-010-9507-4.

Mishuris, G.S., Movchan, A.B., Slepyan, L.I., 2009. Origin of crack tip instabilities. J. Mech. Phys. Solids 57, 1958–1979. http://dx.doi.org/10.1016/j.jmps.2009.08.004.

Mishuris, G.S., Movchan, A.B., Slepyan, L.I., 2019. Waves in elastic bodies with discrete and continuous dynamic microstructure. Phil. Trans. R. Soc. A 378, 20190313. http://dx.doi.org/10.1098/rsta.2019.0313.

Mitchell, N.P., Nash, L.M., Irvine, W.T.M., 2018. Tunable band topology in gyroscopic lattices. Phys. Rev. B 98, 174301. http://dx.doi.org/10.1103/PhysRevB.98.174301.

Movchan, A.B., Movchan, N., Haq, S., 2006. Localised vibration modes and stop bands for continuous and discrete periodic structures. Mater. Sci. Eng. A 431 (1-2), 175–183. http://dx.doi.org/10.1016/j.msea.2006.05.145.

Movchan, A.B., Slepyan, L.I., 2007. Band gap Green's functions and localized oscillations. Proc. R. Soc. Lond. Ser. A Math. Phys. Eng. Sci. 463, 2709–2727. http://dx.doi.org/10.1098/rspa.2007.0007.

Nash, L.M., Kleckner, D., Read, A., Vitelli, V., Turner, A.M., Irvine, W.T.M., 2015. Topological mechanics of gyroscopic metamaterials. Proc. Natl. Acad. Sci. 112, 14495–14500. http://dx.doi.org/10.1073/pnas.1507413112.

Nieves, M.J., Carta, G., Pagneux, V., Brun, M., 2020. Rayleigh waves in micro-structured elastic systems: Non-reciprocity and energy symmetry breaking. Int. J. Eng. Sci. 156, 103365. http://dx.doi.org/10.1016/j.ijengsci.2020.103365.

Nieves, M.J., Movchan, A.B., Jones, I.S., 2012. Analytical model of thermal striping for a micro-cracked solid. Int. J. Solids Struct. 49, 1189–1194. http://dx.doi.org/10.1016/j.ijsolstr.2012.01.003.

Nieves, M.J., Movchan, A.B., Jones, I.S., Mishuris, G.S., 2013. Propagation of Slepyan's crack in a non-uniform elastic lattice. J. Mech. Phys. Solids 61, 1464–1488. http://dx.doi.org/10.1016/j.jmps.2012.12.006.

Ostoja-Starzewski, M., 2002. Lattice models in micromechanics. Appl. Mech. Rev. 55 (1), 35–60. http://dx.doi.org/10.1115/1.1432990.

Piccolroaz, A., Mishuris, G.S., Movchan, A.B., 2009. Symmetric and skew-symmetric weight functions in 2D perturbation models for semi-infinite interfacial cracks. J. Mech. Phys. Solids 57, 1657–1682. http://dx.doi.org/10.1016/j.jmps.2009.05.003.

Piccolroaz, A., Mishuris, G.S., Movchan, A.B., 2010. Perturbation of mode III interfacial cracks. Int. J. Fract. 166, 41–51. http://dx.doi.org/10.1007/s10704-010-9484-7.

Piccolroaz, A., Mishuris, G.S., Movchan, A.B., Movchan, N.V., 2012. Mode III crack propagation in a bimaterial plane driven by a channel of small line defects. Comput. Mater. Sci. 64, 239–243. http://dx.doi.org/10.1016/j.commatsci.2012.02.037.

Sharma, B.L., 2017. On linear waveguides of square and triangular lattice strips: an application of Chebyshev polynomials. Sādhanā 42, 901–927. http://dx.doi.org/10.1007/s12046-017-0646-4.

Sharma, B.L., 2018. On linear waveguides of square and triangular lattice strips: an application of Chebyshev polynomials. Waves Random Complex Media 28 (1), 96–138. http://dx.doi.org/10.1080/17455030.2017.1331061.

Sharma, B.L., Eremeyev, V., 2019. Wave transmission across surface interfaces in lattice structures. Int. J. Eng. Sci. 145, 103173. http://dx.doi.org/10.1016/j.ijengsci.2019.103173.

Slepyan, L.I., 2001a. Feeding and dissipative waves in fracture and phase transition: I. Some 1D structures and a square-cell lattice. J. Mech. Phys. Solids 49 (3), 469–511. http://dx.doi.org/10.1016/S0022-5096(00)00064-8.

Slepyan, L.I., 2001b. Feeding and dissipative waves in fracture and phase transition: III. triangular-cell lattice. J. Mech. Phys. Solids 49 (12), 2839–2875. http://dx.doi.org/10.1016/S0022-5096(01)00053-9.

Slepyan, L.I., 2002. Models and Phenomena in Fracture Mechanics. Springer, Berlin, ISBN: 978-3-540-48010-5.

Slepyan, L.I., Movchan, A.B., Mishuris, G.S., 2010. Crack in a lattice waveguide. Int. J. Fract. 162, 91–106. http://dx.doi.org/10.1007/s10704-009-9389-5.

Su, Z., Ye, L., 2021. Identification of Damage using Lamb Waves: From Fundamentals to Applications. In: Lecture Notes in Applied and Computational Mechanics, vol. 48, Springer, Switzerland, http://dx.doi.org/10.1007/978-1-84882-784-4.

Süsstrunk, R., Huber, S.D., 2015. Observation of phononic helical edge states in a mechanical topological insulator. Science 349 (6243), 47–50. http://dx.doi.org/10.1126/science.aab0239.

Tallarico, D., Movchan, N.V., Movchan, A.B., Colquitt, D.J., 2017a. Tilted resonators in a triangular elastic lattice: Chirality, Bloch waves and negative refraction. J. Mech. Phys. Solids 103, 236–256. http://dx.doi.org/10.1016/j.jmps.2017.03.007.

Tallarico, D., Trevisan, A., Movchan, N.V., Movchan, A.B., 2017b. Edge waves and localization in lattices containing tilted resonators. Front. Mater. 4, 16. http://dx.doi.org/10.3389/fmats.2017.00016.

Vadalà, F., Bacigalupo, A., Lepidi, M., Gambarotta, L., 2021. Free and forced wave propagation in beam lattice metamaterials with viscoelastic resonators. Int. J. Mech. Sci. 193, 106129. http://dx.doi.org/10.1016/j.ijmecsci.2020.106129.

Wang, P., Lu, L., Bertoldi, K., 2015. Topological phononic crystals with one-way elastic edge waves. Phys. Rev. Lett. 115, 104302. http://dx.doi.org/10.1103/PhysRevLett.115.104302.

Zhu, X., Zou, X., Liang, B., Cheng, J., 2010. One-way mode transmission in one-dimensional phononic crystal plates. J. Appl. Phys. 108, 124909. http://dx.doi.org/10.1063/1.3520491.